Melt transport and mantle assimilation at Atlantis Massif (IODP Site U1309): Constraints from geochemical modeling

Carlotta Ferrando [a,*], Marguerite Godard [a], Benoit Ildefonse [a], Elisabetta Rampone [b]

[a] Géosciences Montpellier, Univ. Montpellier, CNRS, 34095 Montpellier cedex 05, France
[b] DISTAV, University of Genova, Corso Europa 26, I-16132 Genova, Italy

ARTICLE INFO

ABSTRACT

Olivine-rich troctolites (>70% olivine) reveal that extensive melt impregnation of pre-existing olivine-rich lithologies participate to the building of slow spread oceanic crust. To constrain their origin and their impact on the structure and geochemistry of oceanic crust, we realized a multi-scale petro-structural, geochemical, and numerical modeling study of olivine-rich troctolites drilled at IODP Hole U1309D (Atlantis Massif, Mid-Atlantic Ridge 30°N). Discrete intervals of olivine-rich troctolites display sharp to diffuse contacts with neighboring troctolites or gabbros. Their texture is characterized by plastically deformed (high temperature imprint), corroded coarse-grained to undeformed fine-grained olivine embayed in poikilitic clinopyroxene and plagioclase. Olivine crystallographic preferred orientations show weak [001] clusters. Olivine has variable major and minor element compositions, but similar fractionated REE (Dy_N/Yb_N = 0.04–0.11). We distinguished three types of olivine-rich troctolites based on microstructure, texture and mineral composition. Olivine-rich troctolites 1 and 2 display sharp contacts with adjacent lithologies. Type 1 has modal olivine <75%, occurring mainly as single rounded grains with primitive compositions (Mg# = 85–86), and associated with high Mg# clinopyroxene. Type 2 has higher olivine modes (>75%), dominantly forming aggregates, showing more evolved compositions (Mg# = 83–84) and associated with slightly lower Mg# clinopyroxene. These variations of olivine modes and compositions are in contrast to common trends of magmatic crystallization that predicts decreasing modal olivine with melt differentiation towards evolved compositions. Type 3 has diffuse contacts with gabbroic veins and modal olivine overlapping those of types 1 and 2. Chemical traverses along principal crystallographic axes of olivine are flat, suggesting local equilibrium between olivine and neighboring phases. Mineral modes and compositions, together with textures and microstructures, suggest that olivine-rich troctolites formed after melt-rock interactions in a reactive porous flow process. Their compositions are best modeled by percolation of primitive MORBs into Hole U1309D impregnated and compositionally heterogeneous harzburgites, triggering orthopyroxene dissolution, followed by olivine assimilation and concomitant crystallization of clinopyroxene and plagioclase. Modeling shows that Ni variations in olivine at constant Mg# are mantle inherited. Compositions of olivine-rich troctolite 1 are fitted assuming higher olivine assimilation (M_a = 0.06–0.13) in contrast to olivine-rich troctolites 2 and 3 (M_a = 0.01–0.02). Olivine-rich troctolite 3 was 'buffered' by crystallizing reacted melts, progressively more evolved as temperature decreased during a late stage process. We interpret olivine-rich troctolites from the Atlantis Massif as marking local assimilation of harzburgitic mantle into the gabbroic sequence during a period of enhanced magmatism at depth. Our study shows that the distribution and variable compositions of olivine-rich troctolites result from the incipient stages of this process when local spatial variations in mantle rock permeability, probably related to pyroxene distribution, controlled in turn melt transport and mantle-melt interactions.

1. Introduction

The formation of oceanic crust by partial melting of upwelling asthenosphere at mid-ocean ridges represents one of the main outcomes of mantle geodynamics at the surface of the Earth. The architecture of oceanic crust varies from "layered", characterized by a volcanic basaltic crust that overlies a lower crustal plutonic (gabbroic) sequence, to the "heterogeneous" formed by serpentinized peridotites intruded by gabbroic bodies and overlain by a thin or absent extrusive section (e.g., review in Coogan, 2014). Both architectures are observed along slow-spreading ridges while the former is dominant along fast-spreading centers (e.g., review in Coogan, 2014). The composition of the

* Corresponding author at: Géosciences Montpellier (UM 5243 - CNRS), Université de Montpellier, cc60, Place Eugene Bataillon, 34095 Montpellier cedex 5, France.
E-mail address: ottaferrando@gmail.com (C. Ferrando).

oceanic crust is commonly modeled as the product of fractional crystallization of primary mantle melts, forming the tholeiitic differentiation suite: dunite → troctolite (and wehrlite) → olivine gabbro → gabbro → basalt (e.g., Bowen, 1928; Gast, 1968). Accordingly, and based on early petrological studies that allowed to predict the effects of this fractional crystallization suite on the composition of basalts (e.g., O'Hara, 1965; Shaw, 1970), Mid-Ocean Ridge Basalts (MORB) have been used extensively to determine the composition of their mantle source as well as the conditions and extent of melting that led to their formation (e.g., Elthon, 1979; Grove et al., 1992; O'Neill and Jenner, 2012). Yet, petrographic observations and geochemical studies of oceanic plutonic sequences show that fractional crystallization may not uniquely account for the composition and textures of gabbroic series, thus challenging this simple differentiation model.

Textures of gabbroic rocks commonly show corroded grain boundaries of early crystallized minerals and the occurrence of interstitial phases (e.g., Holness et al., 2007), suggesting chemical reaction of the crystal mush with an interstitial melt. These textural features indicate disequilibrium among phases. On the other hand, chemical equilibrium between phases is observed for major elements, in particular for the most primitive end-members of gabbroic series (e.g., Langmuir, 1989; Lissenberg and Dick, 2008). Nevertheless, trace elements are in disequilibrium between coexisting phases (e.g., Drouin et al., 2009; Rampone et al., 2016) and display significant enrichments compared to those predicted by fractionation trends (e.g., Bédard, 1993; DePaolo, 1981; O'Hara, 1977). These observations have been interpreted as the result of 'open-system' processes including periodic melt injection and mineral assimilation. Chemical exchanges between a pre-existing crystal matrix and exotic melts (e.g., Bédard et al., 2000; Dick et al., 2000; Kvassnes and Grove, 2008; Lissenberg et al., 2013; Renna et al., 2016) or postcumulus reactions with late-stage interstitial melts (e.g., Borghini and Rampone, 2007) have been proposed as mechanisms able to modify the mineral chemistry of primary phases. Also, such reactions may in turn modify the composition of the reacting MORB-type melts (e.g., Lissenberg and Dick, 2008). Natural samples (e.g., Lissenberg et al., 2013; Lissenberg and Dick, 2008; Rampone et al., 2016; Sanfilippo et al., 2015, 2015) and experimental studies (e.g., Lambart et al., 2009; Van den Bleeken et al., 2011) point to a possibly important role of melt-rock interactions in the formation of the oceanic crust.

Olivine-rich troctolites represent the most primitive end-member of gabbroic rocks in the tholeiitic suite of the oceanic crust. They have >70% olivine modal contents, which approach that of dunites, but contain plagioclase and clinopyroxene. They were first described in intracontinental layered intrusions (e.g., 'feldspathic peridotite' and troctolite, Holness et al., 2007; O'Driscoll et al., 2007). Because their textures are distinguished by subhedral to rounded olivine grains embayed in large interstitial plagioclase and clinopyroxene crystals (e.g., Holness et al., 2007) and have rather primitive major element compositions (e.g., O'Driscoll et al., 2007), olivine-rich troctolites were interpreted first as products of magmatic crystallization and melt-rock reactions during replenishment of the magma chamber, or with melts from the host gabbros (e.g., Bédard, 2015 and references therein). Olivine-rich troctolites have also been observed at the mantle–crust transition zone of modern and paleo fast-spreading ridges (e.g., 'plagioclase-bearing dunite' and troctolite, Arai and Matsukage, 1996; Boudier and Nicolas, 1995). They contain olivines that display microstructures consistent with high temperature deformation by dislocation creep, as commonly described in mantle peridotites (Boudier and Nicolas, 1995). They also show chemical variations inconsistent with fractionation trends (e.g., Arai et al., 1997). These olivine-rich troctolites are interpreted as mantle rocks, which composition and texture were modified as the result of extensive melt impregnation atop the upwelling mantle at the mantle-crust transition along spreading ridges (e.g., Boudier and Nicolas, 1995; Dijkstra et al., 2003; Higgie and Tommasi, 2012). More recently, intervals of olivine-rich troctolites have been extensively observed

interlayered within the heterogeneous oceanic crust at modern slow-spreading ridges (e.g., Drouin et al., 2009, 2010; Sanfilippo et al., 2015; Suhr et al., 2008) and ophiolite analogues (e.g., Rampone et al., 2016; Renna et al., 2016; Sanfilippo et al., 2014, 2015). These olivine-rich troctolites present textures similar to the "feldspathic peridotite and troctolite" of large layered intrusions and of thick plutonic lenses, which formed after a cumulate protolith (e.g., O'Driscoll et al., 2007; Renna et al., 2016). However, they also show selective enrichments in the most incompatible elements generally interpreted as evidence of a melt-rock interaction (e.g., Basch et al., 2018; Drouin et al., 2009; Rampone et al., 2016; Sanfilippo et al., 2014). Finally, some of these olivine-rich troctolites show textures and microstructures of high temperature deformation similar to those formed at the mantle-crust transition zone (Drouin et al., 2010), suggesting that the precursor material is of mantle origin (e.g., Basch et al., 2018; Drouin et al., 2009, 2010; Sanfilippo et al., 2015, 2015; Sanfilippo and Tribuzio, 2013, 2011).

A reactive origin for the olivine-rich troctolites from modern slow-spread oceanic crust was first proposed following the studies of the heterogeneous gabbroic sequence exposed by detachment faulting at the Atlantis Massif (Drouin et al., 2009, 2010; Suhr et al., 2008). Discrete intervals of olivine-rich troctolites were recovered in IODP Hole U1309D (30°N, Mid-Atlantic Ridge (MAR), Expeditions 304/305; e.g., Blackman et al., 2011 and references therein). Because of their microstructural and textural similarities with impregnated peridotites, together with their mineral compositions inconsistent with a simple process of fractional crystallization, Drouin et al. (2009, 2010) and Suhr et al. (2008) inferred that olivine-rich troctolites from Hole U1309D could originally represent mantle relicts. Nevertheless, no unequivocal argument sustains this hypothesis, and the nature of the olivine-rich precursor remains to date unresolved (e.g., Drouin et al., 2009, 2010; Renna et al., 2016). In this contribution, we present a detailed multi-scale petro-structural and geochemical study of olivine-rich troctolites drilled at IODP Hole U1309D. Our purpose is to investigate the mechanisms driving melt-rock interaction processes and ultimately identify the origin of these olivine-rich troctolites. For the first time, we reproduce the chemical compositions of olivines from olivine-rich troctolites using numerical modeling to simulate processes of melt-rock reactions combined with the effects of melt transport ('Plate Model' proposed by Vernières et al., 1997).

2. Geological setting and sample selection

The Atlantis Massif is located at 30°N on the western flank of the slow spreading Mid-Atlantic Ridge (MAR), at the inside corner of the intersection with the Atlantis transform fault (Fig. 1). The corrugated core of the domal massif is a ~2 Ma old Oceanic Core Complex (OCC) that extends over an area approximately 8–10 km wide and 15 km long. Lower crust and upper mantle rocks are exposed via a long-lived and low-angle detachment fault (e.g., Blackman et al., 2002, 2011; Cann et al., 1997; Ildefonse et al., 2007) that spreads at an average (fault slip) rate of 26 mm/yr (Grimes et al., 2008).

IODP Hole U1309D, the deepest hole drilled at Atlantis Massif (Fig. 1), penetrated 1415.5 m below sea floor (mbsf). The recovered section is a highly heterogeneous gabbroic sequence (93.7% of oxide gabbro, gabbro, olivine-gabbro, and troctolite), with MORB-type diabase intrusions (2.9% of the recovered rocks) sampled dominantly in the upper 130 m (Blackman et al., 2011; Godard et al., 2009). Structural and geochemical investigations indicate that the crustal section at Site U1309 record a complex intrusive history, and was formed by multiple magmatic injections over a minimum accretion time of 200 (±120) ka (Blackman et al., 2011; Grimes et al., 2008). Three major intrusive events were identified. For this study, we focus on the deepest crust interval that occurs below 600 mbsf. Constraints from $^{206}Pb/^{238}U$ zircon ages from oxide gabbros and leucocratic dykes indicate that the interval between 600 and 1235 mbsf represent the oldest intrusive event at
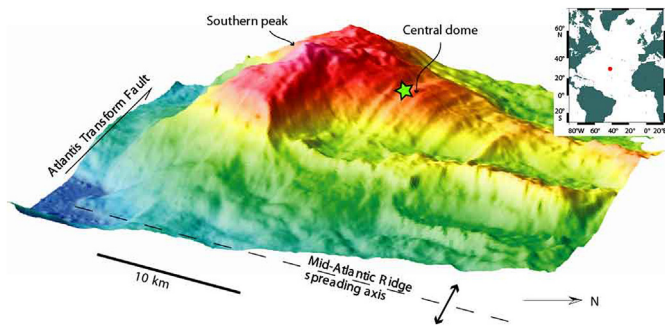
Fig. 1. 3D reconstruction of Atlantis Massif OCC (looking W) modified after Blackman et al. (2002). The green star indicates the location of IODP Hole U1309D on the corrugated detachment fault surface of central dome.

~1.24 Ma (Grimes et al., 2008). The vertical accretion of this section occurred by emplacement of multiple sills at ~7 km depth (Grimes et al., 2008).

The most primitive intervals have variable thicknesses and were recovered at different depths within the gabbroic sequence (Blackman et al., 2011). They comprise minor mantle peridotites (≪1% of total core) and 5.4% (total core) of olivine-rich troctolites observed in 22 discrete intervals throughout the core. The altered mantle relicts are impregnated residual harzburgite screens (Godard et al., 2009; Tamura et al., 2008) crosscut by gabbroic dikelets; they were recovered in the upper ~200 m at Holes U1309B and U1309D. Along slow spreading ridges, the formation of heterogeneous oceanic crust, made of serpentinized mantle rocks intruded by discrete gabbroic bodies and exposed on the seafloor, is interpreted as related to low magma supply (e.g., Cannat et al., 1995; Dick, 1989).

Groundmass alteration at Hole U1309D is moderate and decreases downhole (Blackman et al., 2011). We selected for this study the

interval between 1100 and 1300 mbsf where olivine-rich troctolite is the dominant lithology, and is locally very fresh with <1% serpentinization (Figs. 2 and 3). We collected a total of 15 olivine-rich troctolites: 1 sample at 1096 mbsf, 2 samples at 1125–1160 mbsf, 9 samples at 1190–1193 mbsf, and 3 samples at ~1195 mbsf. Three samples were collected in contact with gabbroic veins, at 1190.5 and 1193.5 mbsf. In order to compare the composition of olivine-rich troctolites with a magmatic end-member we also collected a troctolite at 1290 mbsf.

3. Petrologic overview of U1309D olivine-rich troctolites

Shipboard data and previous on-shore petrologic and geochemical studies provide a first order characterization of the meter-scale downhole variability of the gabbroic sequence recovered at IODP Hole U1309D on the Atlantis Massif OCC (e.g., Blackman et al., 2011; Godard et al., 2009; Grimes et al., 2008; Miller et al., 2009). In contrast to what is described at Atlantis Bank, SW Indian Ridge (Dick et al., 2000), downhole chemical compositions show no significant crystallization trends throughout Hole U1309D (e.g., interval 1100–1300 mbsf in Fig. 2). Here, we summarize the principal characteristics of U1309D olivine-rich troctolites.

During IODP Expedition 304/305 olivine-rich troctolites (Ol-T; >70% modal olivine, Blackman et al., 2006) were sampled in four main interfingered petrologic units within the gabbroic sequence, where they occur as ~40 cm to ~12 m thick discrete intervals crosscut by relatively more evolved gabbroic rocks. Overall, the contacts between Ol-T and troctolitic or gabbroic intervals are sharp, displaying no progressive modal variations. Throughout Hole U1309D, at the scale of few cm to a few dm, Ol-T are heterogeneous in composition (Fig. 3c), varying from dunite (>90 vol% olivine at macroscopic to thin section scale and 10 vol% plagioclase, with <1 vol% clinopyroxene) to troctolite (~70 vol% olivine and ~30 vol% plagioclase) and wehrlite (~70 vol% olivine and ~30 vol% clinopyroxene).
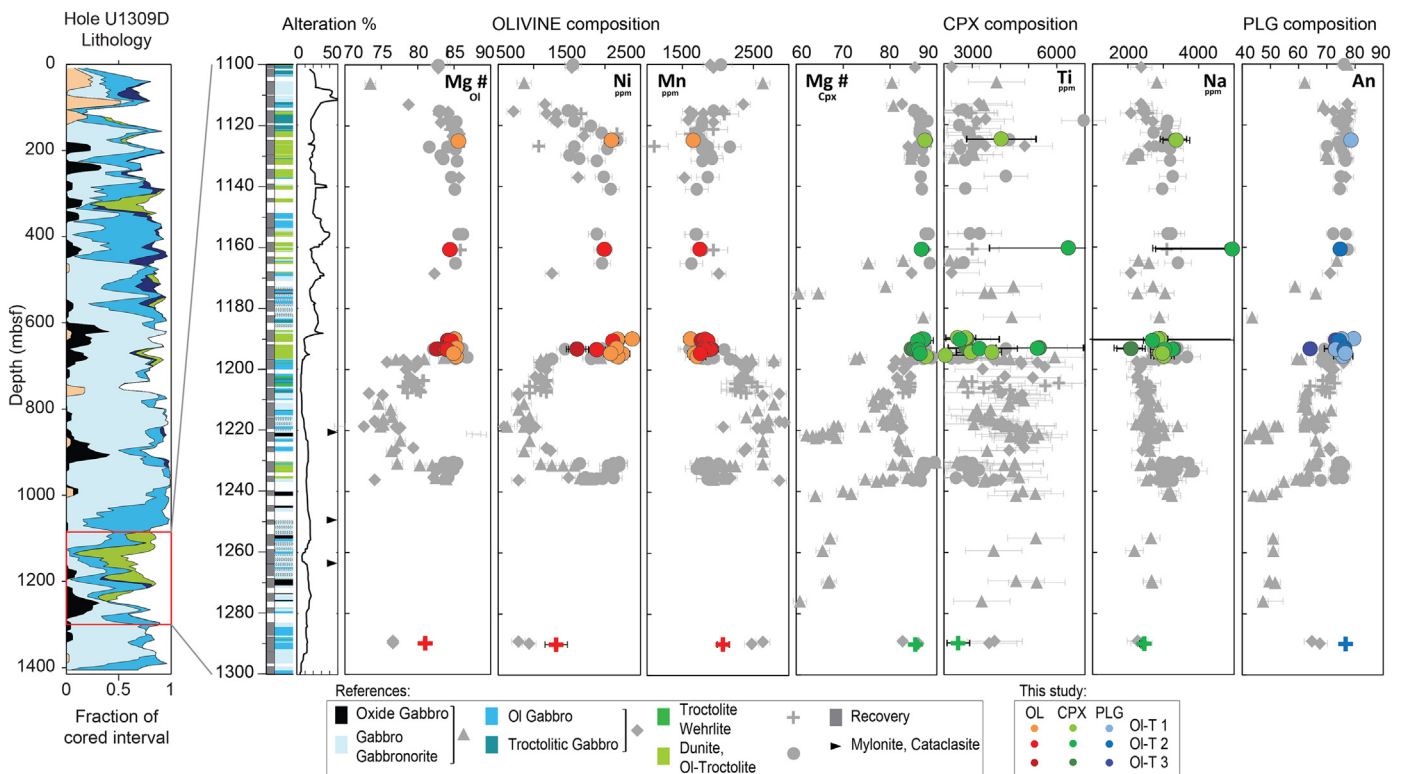

Fig. 2. Olivine (Mg#, Ni, Mn), clinopyroxene (Mg#, Ti, Na) and plagioclase (An) compositions of analysed samples in the interval 1100–1300 mbsf. Recovery, lithology and alteration logs are reported after Blackman et al. (2006). Colored dots represent single samples analysed in this study. Grey symbols indicate data from previous studies (Drouin et al., 2009; Miller et al., 2009; Suhr et al., 2008).
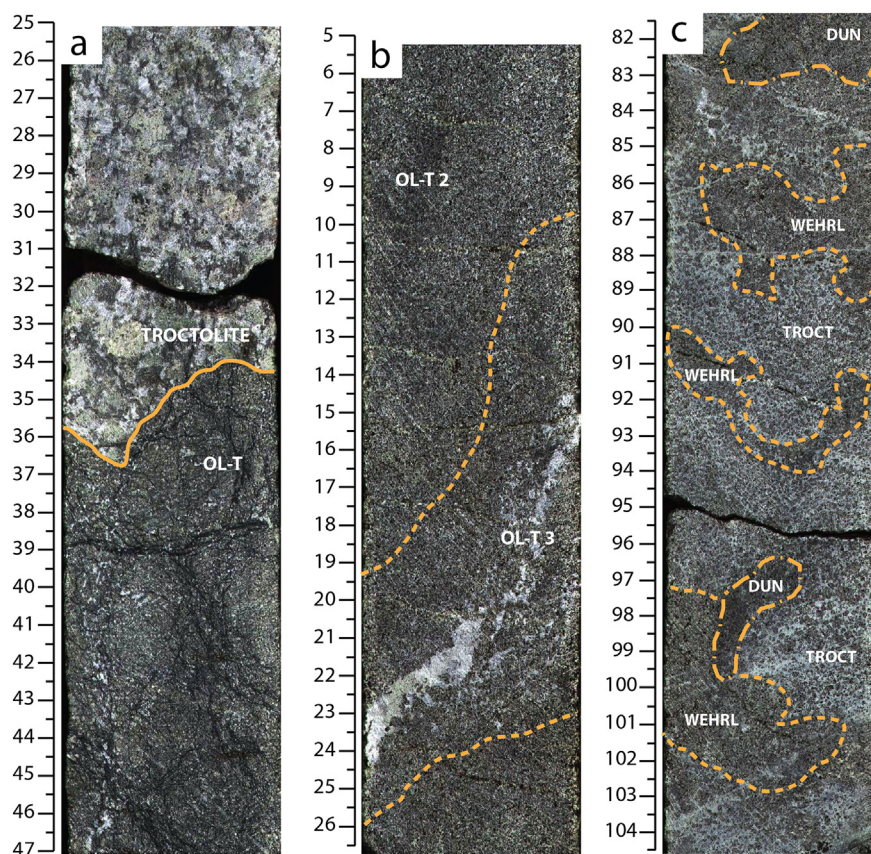
Fig. 3. Examples of (a–b) recovered contacts between Ol-T and gabbro, and (c) interval of heterogeneous Ol-T. a) Core 227R-2, 25–47 cm shows sharp and irregular (in orientation) contact with troctolite. b) Core 248R-2, 5–26 cm shows Ol-T2 (see text) cut by a gabbroic vein; contacts are diffuse and record an increase in modal plagioclase from the core of Ol-T2 to the contact. This Ol-T - gabbro boundary is an example of Ol-T3. c) Core 248R-3, 82–104 cm is an example of Ol-T1 composed of wehrlitic (WEHRL), troctolitic (TROCT) and minor dunitic (DUN) domains.

Ol-T display poikilitic textures that are characterized by rounded granular olivines embedded in large and interstitial plagioclase and/or clinopyroxene crystals, which resemble homogeneous cumulate-like textures described in layered intrusions (e.g., Rum cumulate series; Holness et al., 2007). Nevertheless, olivine crystals display high-temperature dislocation creep, which is commonly described in mantle peridotites, while plagioclase and clinopyroxene show no deformation signature (Drouin et al., 2010). Yet, most Ol-T samples display crystallographic preferred orientation (CPO) of olivine with relatively stronger clustering of [001] crystallographic axes compared to the [100] and [010] axes (Drouin et al., 2010); this feature contrasts with the axial [100] fabrics typically observed for mantle olivine (e.g., Tommasi et al., 2000).

Bulk rock chemical data show that Ol-T are the most primitive crustal rock cored at Atlantis Massif with high bulk Mg# (Mg# = $100 \times$ cationic Mg/(Mg + Fe$_{TOT}$) with all Fe (Fe$_{TOT}$) calculated as Fe^{2+}) of ~86 (in comparison with Mg# 81 of olivine gabbros; Godard et al., 2009). Olivine in Ol-T is characterized by relatively primitive compositions (Fo$_{82}$ to Fo$_{88}$; Drouin et al., 2009; Miller et al., 2009; Suhr et al., 2008) in contrast to gabbros and olivine gabbros that display lower forsterite contents (down to Fo$_{72}$; Miller et al., 2009; Fig. 2). Plagioclase has anorthitic composition in most recovered rocks (An$_{65}$–An$_{82}$; Miller et al., 2009; Drouin et al., 2009; Fig. 2), and clinopyroxene has generally high Mg# (75–90; Drouin et al., 2009; Miller et al., 2009; Suhr et al., 2008; Fig. 2). Trace elements (i.e., REE) in plagioclase and clinopyroxene from Ol-T are in equilibrium, whereas olivine is in chemical disequilibrium with both interstitial phases (Drouin et al., 2009). The absence of systematic modal variations between Ol-T and gabbro, together with the microstructures of Ol-T (Drouin et al., 2010), analyses of bulk rock compositions (Godard et al., 2009), and mineral chemical disequilibrium (Drouin

et al., 2009), were interpreted as evidence that Ol-T at the Atlantis Massif are the result of a multi-stage melt impregnation process through an olivine-rich precursor (Drouin et al., 2009, 2010; Suhr et al., 2008).

4. Analytical methods

In order to document the scale of modal and chemical heterogeneities in Hole U1309D rocks, in particular Ol-T, the most relevant intervals were described in detail at the Bremen Core Repository. A first set of samples were selected from those used in Drouin et al. (2009), and a second set at the Bremen Core Repository.

Olivine, pyroxene and plagioclase CPO in most of the studied core intervals were provided by Drouin et al. (2010). We report complementary analyses of microstructures (morphological textures) and new data of in situ major and trace element compositions for olivine, plagioclase and clinopyroxene. Petro-geochemical profiles were done along preferred directions selected parallel to (at least) one of the three principal crystallographic axis of olivine, as defined by microstructural analysis. Plagioclase and clinopyroxene were analysed along the same profiles, in prolongation of the preferred direction in adjacent olivine crystals.

Microstructures were analytically characterized by indexation of Electron Backscattered Diffraction (EBSD) measurements using the SEM-EBSD facilities at Geosciences Montpellier (University of Montpellier). A set of 8 Ol-T was analysed by a Scanning Electron Microscope (SEM) JEOL JSM 5600, and another set of 7 samples of Ol-T and 1 troctolite were analysed by a Field Emission Gun (FEG) CamScan X500FE CrystalProbe. Operating conditions and data processing are given in the Supplementary Material - analytical methods and models.

Major element compositions of minerals were determined by Electron Probe Micro Analyser (EPMA) at Geosciences Montpellier

(University of Montpellier), using a CAMECA SX100 equipped with five wavelength-dispersive X-ray spectrometers (WDS). Analyses were done with 20 kV accelerating potential, 10 nA beam current and 30 s counting times for all elements measured. Natural minerals and synthetic oxides are used as standards.

In situ trace element compositions were determined at Geosciences Montpellier, using a Thermo Scientific Element 2XR (eXtended Range) high resolution - Inductively Coupled Plasma Mass Spectrometry (ICP-MS). The ICP-MS is coupled with laser ablation (LA) system, a Microlas (Geolas Q+) automated platform with a 193 nm Excimer Compex 102 laser from LambdaPhysik. The laser energy density was set to 12–15 J cm² and repetition rate at 8–10 Hz. The laser spot size was set to 102–77 μm for olivine, and 77 μm for plagioclase and clinopyroxene. Data were reduced with the GLITTER software package (Van Achterbergh et al., 2001), using the linear fit to ratio method. Concentrations were calibrated against the NIST 612 rhyolitic glass using the values given in Pearce et al. (1997). ^{29}Si for olivine and ^{43}Ca for plagioclase and pyroxenes were used for internal standardization relative to EPMA data. The sample preparation and methods for data acquisition and reduction are detailed in the Supplementary Material - analytical methods and models - together with the precision and accuracy of the LA-ICP-MS analyses and the values obtained for standard reference basalt BIR-1G (Supplementary Material Table S3).

Compositions of olivine, plagioclase and clinopyroxene are in Supplementary Material Tables S1 and S2.

5. Results

5.1. Downhole characteristics of olivine-rich troctolites in the 1100–1300 mbsf interval

Ol-T is the dominant lithology between 1100 and 1300 mbsf of Hole U1309D. Contacts with neighbouring gabbros were recovered at different depths. Based on interval thickness and contact morphology, two main structural relationships are identified (Fig. 3a–b). A first feature is defined by dm to several m thick gabbroic intervals that cut Ol-T with sharp contacts (Fig. 3a). The >1 m thick gabbro intervals display regularly distributed modal composition and grain size variations, in contrast to cross-cut olivine-rich intervals that have either constant modal composition or irregularly distributed olivine modal contents. The second structural feature consists in 2 to 5 cm thick gabbroic veins (olivine <5 vol%) that show diffuse contacts with the Ol-T. These contacts display higher plagioclase modal contents progressively

decreasing with increasing distance from the gabbroic vein, forming a plagioclase-rich halo of maximum 5 cm thickness within the Ol-T (Fig. 3b).

Ol-T in the top 90 m of 1100–1300 mbsf interval have ~70–80 vol% modal olivine and variable modal content of poikilitic interstitial phases, with clinopyroxene/plagioclase modal ratio between 0.4 and 1 (Table 1). Domains with >75 vol% modal olivine dominate between 1190 and 1193 mbsf, where local enrichments in plagioclase and minor clinopyroxene (up to ~25 vol% of plg) are shown. At 1193–1194 mbsf (Core U1309D-248R) olivine decreases downhole, while clinopyroxene content increases at the expense of olivine and plagioclase up to clinopyroxene/plagioclase ratio of 1 (Table 1). Except for this interval, no downhole correlations with depth are observed for compositional variations in Ol-T (Blackman et al., 2006).

In all studied Ol-T samples, two textural occurrences of olivine crystals are distinguished based on their morphology and deformation signature. The first type is formed by coarse to medium grained olivine crystals displaying well-defined and widely-spaced subgrain boundaries (Fig. 4d,f), and partially corroded grain boundaries. Incipient olivine dissolution is often observed at intersections between grain and subgrain boundaries (Fig. 4f). This type of deformed olivine corresponds to the olivine described by Drouin et al. (2010) as recording high temperature deformation signature. The second type comprises fine grained rounded olivine chadacrysts with no evidence of deformation (Fig. 4c,e) and, in few instances, forming chains of grains in near optical continuity. These undeformed olivines are interpreted as being formed after corrosion and disruption along grain and subgrain boundaries of pre-existing (deformed) coarse grained olivines (Drouin et al., 2010).

Ol-Ts dominated by wehrlitic and troctolitic domains (cpx/plg ratio = 0.5–1, Table 1) contain 64–77 vol% modal olivine (Figs. 3c and 4a), whereas Ol-Ts with 77–84 vol% modal olivine show mainly dunitic domains and plagioclase is the dominant interstitial phase (cpx/plg =0.15–0.46, Table 1; Figs. 3b and 4b). The former are characterized by olivines with Mg# ranging from 85 to 85.6 and the latters have olivines showing lower Mg# (84–84.6, Table 1). Ol-Ts with lower olivine modal contents predominantly show medium interstitial (in the range 0.3–1 mm) to large poikilitic (1–2 mm) grains of plagioclase and clinopyroxene (Fig. 4a) having An contents between 75 and 79.4, and Mg# ranging from 86.4 to 87.6, respectively (Supplementary Material Table S1). Plagioclase and clinopyroxene in Ol-Ts with higher modal olivine are mainly small (<300 μm) interstitial grains (Fig. 4b) that have An contents in the range 64–75, and

Table 1

List of samples and their principal textural characteristics and mineral chemical compositions. Ol = olivine, Cpx = clinopyroxene, Plg = plagioclase, Opx = orthopyroxene. Mg# = 100 × cationic (Mg/(Mg + Fe), with all Fe as Fe^{2+}.

| Sample IODP	Depth (mbsf)	Lithology	Core description			Thin section description							
						Mineral modes (% of EBSD indexed points)					Mineral chemistry		
			Tot Alteration %	Cpx/Plg	Ol/Cpx + Ol	Ol	Spl	Plg	Cpx	Opx	Mg# Ol	An Plg	Mg# Cpx
305-U1309D-227R-3W, 124–126	1096.17	Ol Troctolite 2	20	0.41	0.91	77	0	15	8	–	84.0	78.9	87.6
305-U1309D-234R-1W, 22–26	1124.97	Ol Troctolite 1	70	0.48	0.88	75	0	22	3	–	85.6	78.5	87.4
305-U1309D-241R-2W, 89–91	1160.66	Ol Troctolite 2	10	0.27	0.96	84	0	13	3	–	84.4	74.7	86.6
305-U1309D-247R-3W, 16–18	1190.05	Ol Troctolite 1	5	0.97	0.72	69	0	7	24	0	85.0	79.4	86.7
305-U1309D-247R-3W, 22–25	1190.11	Ol Troctolite 1	5	0.51	0.88	71	0	24	4	–	85.0	75.2	87.1
305-U1309D-247R-3W, 62–66	1190.51	Ol Troctolite 3	10	0.98	0.92	79	0	2	19	0	84.1	73.1	87.0
305-U1309D-247R-3W, 76–81	1190.65	Ol Troctolite 2	10	0.46	0.93	81	–	13	6	–	84.6	74.4	85.8
305-U1309D-248R-1W, 110–113	1193.00	Ol Troctolite 1	5	0.01	0.90	77	0	23	0	–	85.3	76.2	–
305-U1309D-248R-2W, 18–21	1193.32	Ol Troctolite 3	2	0.18	0.93	61	0	33	6	0	82.7	73.0	84.5
305-U1309D-248R-2W, 22–24	1193.36	Ol Troctolite 3	2	0.16	0.98	84	–	10	2	4	82.6	64.1	85.0
305-U1309D-248R-2W, 38–41	1193.52	Ol Troctolite 2	2	0.15	0.97	81	0	17	3	–	84.0	73.1	85.7
305-U1309D-248R-2W, 43–48	1193.57	Ol Troctolite 2	2	0.29	0.95	80	–	16	5	–	84.1	76.1	86.1
305-U1309D-248R-3W, 29–32	1194.78	Ol Troctolite 1	10	0.51	0.87	78	0	18	4	–	85.0	76.5	86.4
305-U1309D-248R-3W, 36–38	1194.85	Ol Troctolite 1	10	0.98	0.70	64	0	6	30	0	85.1	74.7	86.3
305-U1309D-248R-3W, 131–134	1195.80	Ol Troctolite 1	10	0.50	0.89	75	0	20	5	–	85.2	75.7	87.7
305-U1309D-268R-2W, 83–85	1290.06	Troctolite	10	0.85	0.50	34	–	35	30	1	81.0	76.6	85.3
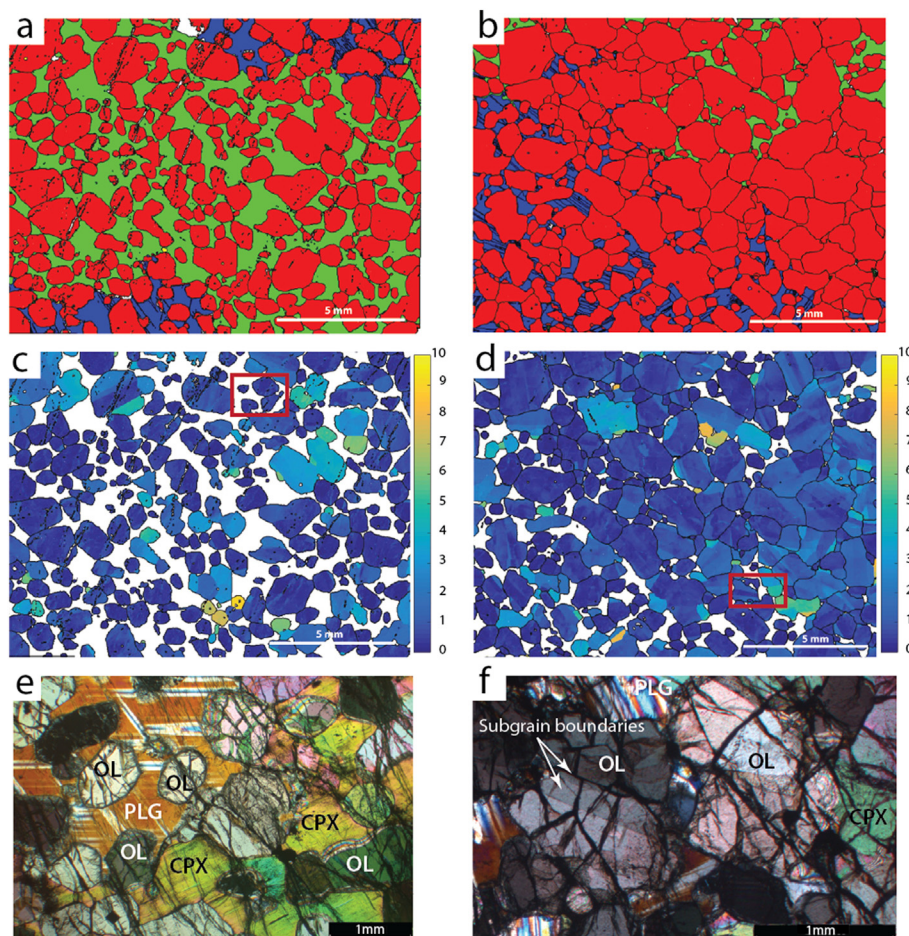
Fig. 4. EBSD processed maps representative of a) and c) Ol-T 1 sample 305-U1309D-247R-3W, 22–25 cm; b) and d) Ol-T2 sample 305-U1309D-248R-2W, 43–48 cm. a)–b) EBSD phase maps where each color corresponds to a phase: red = olivine, blue = plagioclase, green = clinopyroxene. Note single grains embayed in poikilitic interstitial phases in a) Ol-T1, and the abundance of olivine crystals (>75 vol%) forming aggregates in b) Ol-T2. c)–d) Olivine EBSD maps of misorientation to the mean grain orientation, with threshold of misorientation angle for grain boundaries set at 10°. Red rectangles in c) and d) indicate the localization of photomicrographs reported in e) and f), respectively. Microscopic images (cross-polarized light) of e) fine-grained undeformed olivine embayed in poikilitic plagioclase and clinopyroxene (CPX) crystals, and f) medium-grained deformed olivine (OL) showing well defined subgrain boundaries, and corroded grain boundaries in contact with interstitial undeformed plagioclase (PLG).

Mg# between 85 and 86.6 (Supplementary Material Table S1), respectively.

Based on these structural and textural characteristics, and olivine chemical compositions, the studied Ol-Ts were classified in three types. Type 1 and 2 are portions of Ol-T sampled away from their sharp contacts against neighboring gabbros. Type 3 assembles Ol-T collected close to diffuse interfaces with gabbroic veins. Ol-T 1 contains <77 vol% modal olivine (except for one sample with olivine 78 vol%: 305-U1309D-248R-3W, 29–32) with the highest Mg# (Table 1; Figs. 4a,c and 5). Olivine is medium (2–3 mm) to fine (<1 mm) grained (Fig. 4a,c,e). Single olivine grains predominate and are embayed in large poikilitic oikocrysts of plagioclase and clinopyroxene (Fig. 4e). Ol-T 2 contains >77 vol% modal olivine with lower Mg# (Table 1; Figs. 4b,d and 5). Olivine is coarse (5–6 mm) to fine (<1 mm) grained, and forms aggregates of >15 grains (Fig. 4b,d,f). Coarse olivine crystals show lobate grain boundaries against adjacent small interstitial phases, which indicate partial dissolution of olivine by reaction with the melt that crystallized plagioclase and clinopyroxene. In Ol-T 2 plagioclase is the dominant interstitial phase. Ol-T 3 has variable amounts of olivine that overlap with those in Ol-T 1 and Ol-T 2, and the lowest olivine Mg# (82.6–84.1; Table 1). Its composition fills the gap between Ol-T and Troctolite (Fig. 5). Plagioclase has the lowest measured An contents (An_{64}–An_{73}; Table 1) and clinopyroxene display the lowest Mg# (84.5–85 except in sample 305-U1309D-247R-3W, 62–66 with cpx Mg# 87;

Table 1; Fig. 5). Note that orthopyroxene was found in one sample of Ol-T 3, occurring as fine-grained interstitial crystals with Mg# 84. Locally it appears as vermicular grains between olivine and plagioclase or clinopyroxene suggesting that orthopyroxene is not of mantle origin. Instead, it represents the product of late stage crystallization of an evolved melt (e.g., Borghini and Rampone, 2007). This melt concomitantly formed the cross-cutting gabbroic veins.

5.2. Mineral geochemistry

Two groups of elements are distinguished based on their behavior in olivines from Hole U1309D Ol-T. The first group is composed of elements (e.g.,Mg, Fe, Ni, Mn, Zn and Li) that show distinct concentrations in olivines from the three groups of Ol-T. The second group is formed by lithophile trace elements that have similar concentrations in all analysed olivines, and minor variations in plagioclase and clinopyroxene.

The composition of undeformed olivines overlaps that of deformed olivine within the same sample, or does not show systematic variations (Supplementary Material Table S1). Olivine rims display compositions similar to cores (Supplementary Material Table S1). In contrast, clinopyroxene and plagioclase show slight core-rim variations, similar to previously published data (Fig. 3b in Drouin et al., 2009). Such variations are most evident in small interstitial and isolated grains (or wedges) characterized by enrichments in incompatible elements,
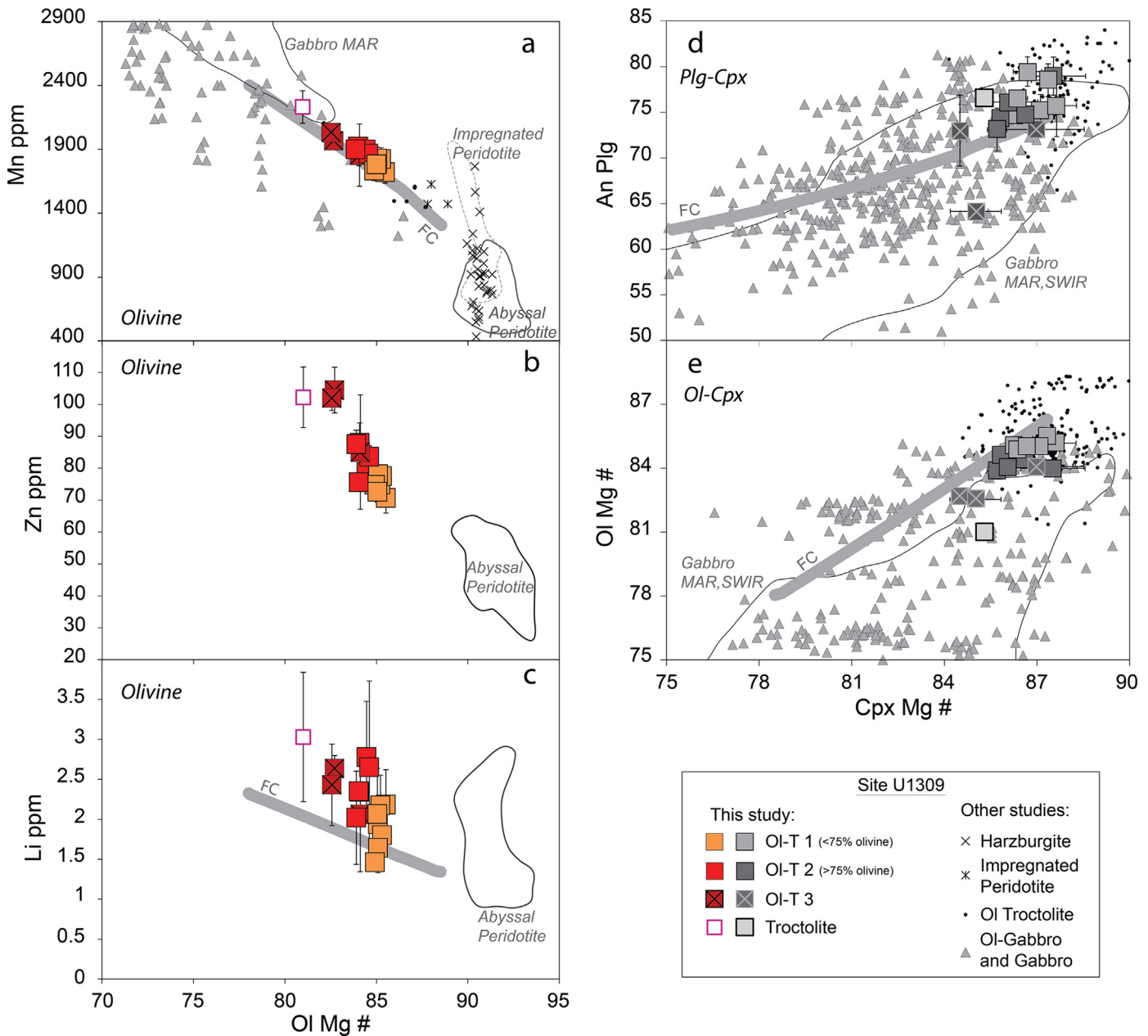
Fig. 5. Olivine (Ol), plagioclase (Plg) and clinopyroxene (Cpx) compositions in Ol-T and troctolite selected from Hole U1309D. Values are reported as sample averages of crystal cores. Olivine Mg# (Mg# = 100 × cationic (Mg/(Mg + Fe)) with all Fe as Fe2+) versus a) Mn (ppm), b) Zn (ppm), c) Li (ppm). Clinopyroxene Mg# versus d) Plagioclase An content (%), e) olivine Mg#. Data from previous studies are reported for comparison: harzburgite and impregnated peridotites from IODP Site U1309 (Miller et al., 2009; Tamura et al., 2008), Ol-T and gabbros from IODP Hole U1309D (Drouin et al., 2009; Miller et al., 2009; Suhr et al., 2008), abyssal peridotites (continuous black line, De Hoog et al., 2010; D'Errico et al., 2016), impregnated peridotites (dotted grey line, Seyler et al., 2007; Tartarotti et al., 2002), gabbros from Mid-Atlantic Ridge (MAR, continuous grey line, Hebert et al., 1991; Ross and Elthon, 1997) and from ODP Hole 735B (SWIR, Dick et al., 2002). The grey thick line in a), c), d), e) indicate major and minor element evolution of mineral element compositions during Fractional Crystallization (FC) of a Primitive MORB Mg# 71 (Presnall and Hoover, 1987). This trend was calculated at 2 kbar pressure using the integrated software Petrolog3 (Danyushevsky and Plechov, 2011). Partition coefficient values are in Supplementary Material Table S4.K_{Mn} was constant during simulation (no significant variations expected). Olivine K_{Li} is from Spandler and O'Neill (2010).

which are associated to lower An contents in plagioclase and lower Mg# in clinopyroxene (Supplementary Material Table S1). These variations were interpreted as resulting from late stage cooling of trapped melt (Drouin et al., 2009).

5.2.1. Minor transition elements and Li in olivine

Olivines have minor transition element compositions higher than those of olivines in abyssal peridotites (MAR 15°N, Seyler et al., 2007; peridotites from other oceanic locations, D'Errico et al., 2016; Tartarotti et al., 2002; Fig. 5a,b), but they are comparable with olivines in impregnated harzburgites (e.g., Site U1309, Miller et al., 2009;

Tamura et al., 2008; Fig. 5a). Mn contents in olivine overlaps compositions of olivines in the most primitive gabbro end-members sampled along the Mid-Atlantic Ridge (IODP Hole U1309D, Drouin et al., 2009; Miller et al., 2009; Suhr et al., 2008; MARK area, Hebert et al., 1991; Lissenberg and Dick, 2008; Ross and Elthon, 1997; Fig. 5a). Li contents are comparable with those of olivines in abyssal peridotites (Fig. 5c). Minor transition elements and Li contents are consistent with the compositional trend predicted for the earlier stages of fractional crystallization, from the most refractory troctolites to olivine depleted gabbros (Villiger et al., 2007): Ni, an element with a strong affinity for olivine (Supplementary Material Table S4), is enriched in high-Mg# olivine

cores (Supplementary Material Table S1), while abundances in elements having moderately incompatible to compatible affinity, such as Mn, Zn and Co ($^{Ol/Melt}K_{Mn} = 1.15$, $^{Ol/Melt}K_{Zn} = 1.16$, $^{Ol/Melt}K_{Co} = 5.21$; Supplementary Material Table S4), display inverse negative correlation with olivine Mg# (Supplementary Material Table S1; Fig. 5).

Ol-T 1 (ol <75%) have olivine with Ni contents ranging from 1870 to 2820 ppm, Mn between 1670 and 1820 ppm, Zn and Li contents in the ranges 70.7–78.0 ppm and 1.5–2.2 ppm, respectively (values are averages per sample; Fig. 5). Olivine in Ol-T 2 (modal ol >75%) is distinguished by lower Ni contents (1790–2130 ppm), coupled with higher Mn (1800–2000 ppm), Zn (75.6–87.9 ppm) and Li contents (2.1–2.9 ppm). Ol-T 3 displays olivine with the lowest Ni contents (1690–2080 ppm), and the highest Mn and Zn contents (Mn = 1850–2030 ppm, Zn = 85.0–104.4 ppm) of all investigated Ol-T (Fig. 5). Li contents of olivines in Ol-T 3 overlap with compositions of Ol-T 2 olivines (Li = 2.06–2.65 ppm). Among all studied samples, troctolite is the most evolved end-member with olivine showing the lowest Ni contents (~1700 ppm), and the highest Mn (~2200 ppm), Zn (~102 ppm) and Li contents (~3 ppm).

These compositions apparently follow a trend of fractional crystallization as predicted at pressure conditions of 2 kbar (~7 km depth as predicted for emplacement of U1309 gabbroic sequence, Grimes et al., 2008; Fig. 5). However, the most primitive chemical compositions are observed in the Ol-T displaying less modal olivine (Ol-T 1; Fig. 5a–c). Extremely variable Ni abundances in olivine at constant Mg# were already highlighted in the previous study of Drouin et al. (2009). Our new geochemical dataset displays similar variations for Li (Fig. 5c), which are not expected after a simple process of fractional

crystallization. Olivine is the major host of Li in mantle peridotites and, usually, do not show strong variations (e.g., De Hoog et al., 2010) in contrast to what observed in the studied olivine crystals.

5.2.2. Lithophile trace elements

Few trace element data are available for olivine in oceanic environments. Most studies focused on olivines from oceanic peridotites (e.g., Gakkel Ridge mantle, D'Errico et al., 2016) and orogenic massifs (e.g., in situ analyses and on separates from Ronda peridotite, Garrido et al., 2000; in situ analyses on Erro-Tobbio ophiolites, Rampone et al., 2016, and Internal Liguride and Pineto ophiolites, Sanfilippo et al., 2014), but gabbroic rocks have been little studied (Site U1309, Drouin et al., 2009; single primitive olivine gabbro from Hess Deep, Lissenberg et al., 2013; Erro-Tobbio olivine gabbros, Rampone et al., 2016).

Olivines from all our samples are on average depleted in lithophile trace elements and have similar trace element contents (Figs. 6a,b and 7a). In Hole U1309D Ol-T, they have Yb_N (N = values normalized to chondrites, after Sun and McDonough, 1989) ranging from 0.18 to 0.78, coupled to strong depletion in M - (medium) REE ($Dy_N = 0.005–0.064$) relative to HREE and scattered L - (light) REE ($La_N = 0.0003–0.006$). Their H - (heavy) REE content are higher than in mantle olivines from abyssal peridotites and mantle ophiolites (Gakkel Ridge, D'Errico et al., 2016; Erro-Tobbio ophiolite, Rampone et al., 2016; Internal Ligurian and Pineto ophiolites, Sanfilippo et al., 2014). The strong normalized H-REE to M- (medium) REE fractionation ($Dy_N/Yb_N = 0.04–0.11$, Fig. 6a,b) that characterizes the studied olivines is similar to what observed in olivine from ophiolitic troctolites (e.g., Rampone et al., 2016; Sanfilippo et al., 2014), and oceanic olivine-rich gabbros (e.g. fast-spreading ridge at
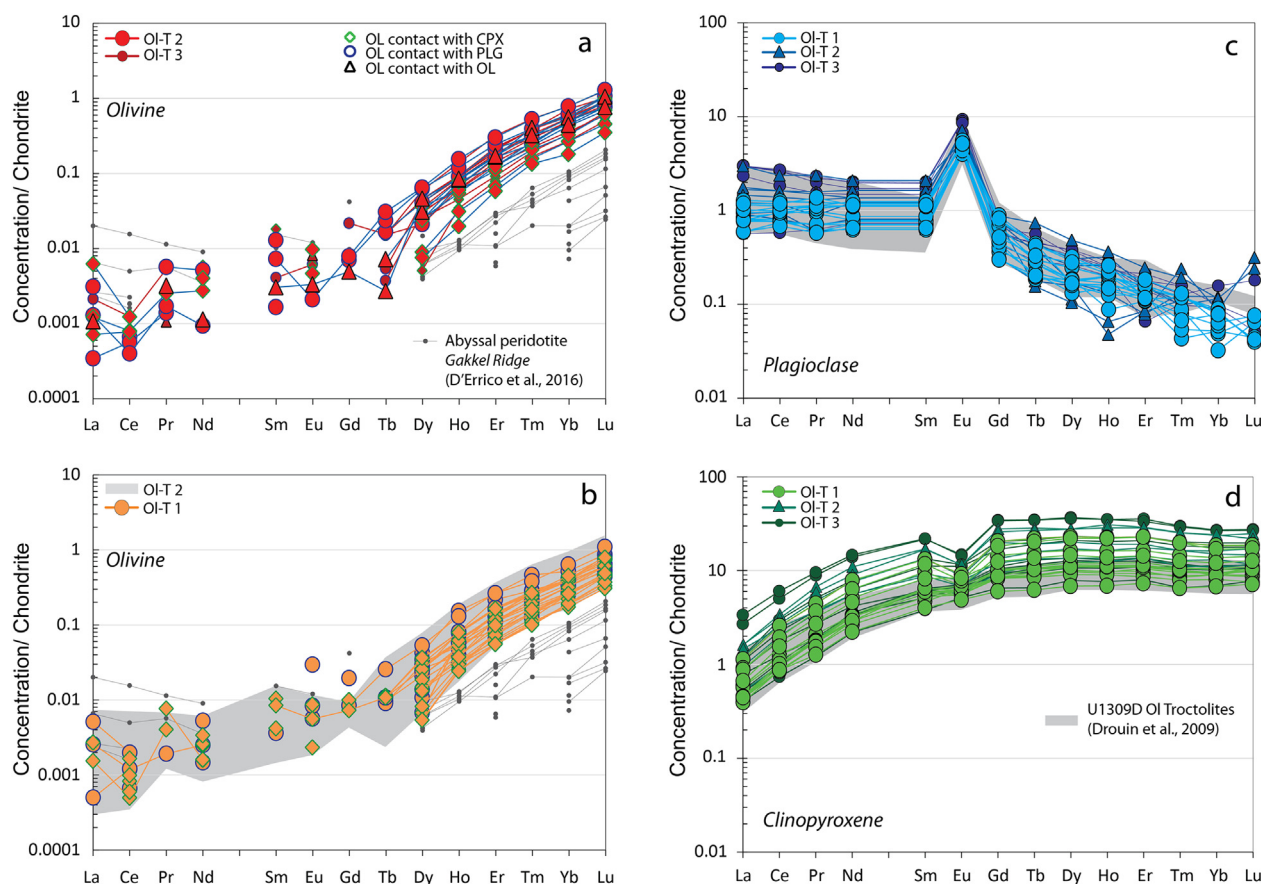

Fig. 6. Chondrite-normalized Rare Earth Element (REE) concentrations of olivine from a) Ol-T2 and Ol-T3 and from b) Ol-T1, of c) plagioclase and d) clinopyroxene from Ol-T of IODP Hole U1309D. REE abundances in olivines from abyssal peridotites of Gakkel Ridge (D'Errico et al., 2016) are shown for comparison in a) and b). REE abundance of Ol-T2 olivine is also represented in b) for comparison. The dark grey fields in c) and d) are REE abundances of plagioclase and clinopyroxene cores in U1309D Ol-T from previous study (Drouin et al., 2009). Symbols refer to phases in contact with analysed olivine (clinopyroxene = CPX, plagioclase = PLG, olivine = OL). Colors in each graph refer to the type of Ol-T. Normalizing values after Sun and McDonough (1989).

Hess Deep, Lissenberg et al., 2013). Within a same sample, olivines embayed in clinopyroxene have lower REE in comparison with olivines in contact with plagioclase.

Extended trace element patterns of olivines highlight positive anomalies in Ti (up to ~110 ppm in olivine-rich troctolites; Ti/Dy = 4–12 X Primitive Mantle-PM) and in the most incompatible High Field Strength Elements (HFSE), such as Zr-Hf and Th-U, relative to the neighboring trace elements (Fig. 7a).

All analysed samples have plagioclase displaying strong Eu positive anomalies (Eu/Eu* = 5–13, except for an Ol-T 1 and an Ol-T 2 with Eu/Eu* = 3.5–5.5). Drouin et al. (2009) showed that plagioclase from U1309D olivine-rich troctolites have comparable compositions to those of oceanic gabbros from the MARK area. All plagioclases have overall comparable REE patterns with La_N/Sm_N ranging between 0.7 and 2 (Fig. 6c). Note that the highest La_N/Sm_N (La_N/Sm_N = 1–2; Fig. 6c) are displayed by plagioclases in Ol-T 2, where they dominantly appear as isolated and small interstitial grains, and Ol-T 3 where they exhibit subhedral habit. Trace element pattern display positive anomalies in Sr and Ti relative to neighboring elements, and negative anomalies in Nb and Zr (Fig. 7b).
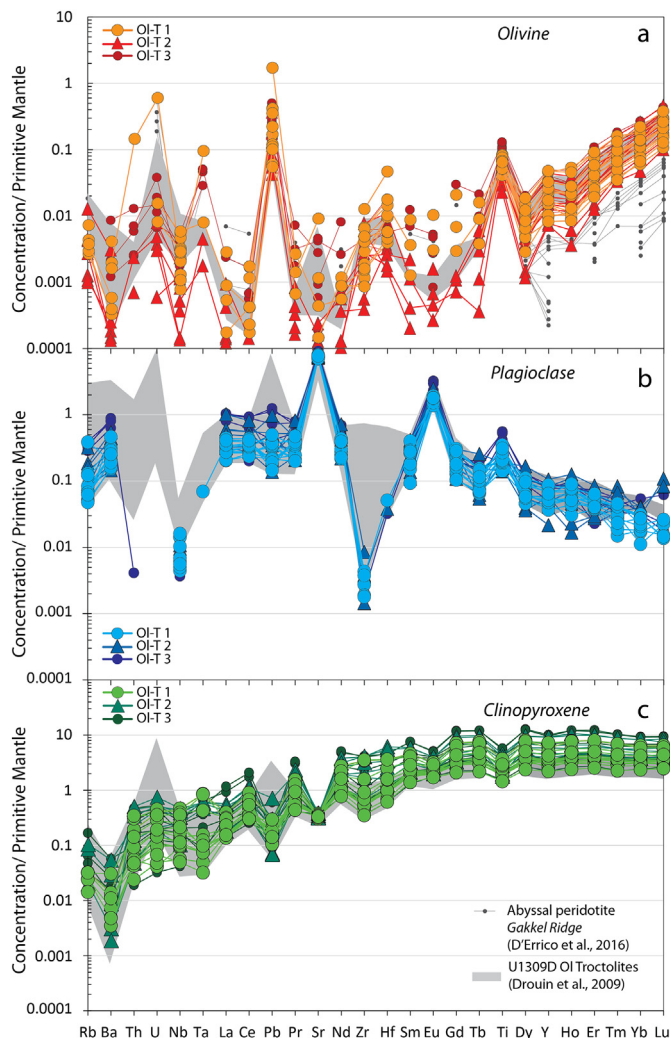
Clinopyroxenes from all investigated Ol-T have compositions similar to those of clinopyroxenes from gabbros sampled along the Mid-Atlantic Ridge (Drouin et al., 2009). They have flat patterns for MREE and HREE and depletion in LREE (La_N/Sm_N = 0.07–0.16, Fig. 6d). They have Yb_N concentrations ranging from 6.7 to 18.5 and Eu/Eu* ratio between 0.7 and ~1 in Ol-T 1. It should be noted that small interstitial clinopyroxene grains in Ol-T 2 and large subhedral grains in Ol-T 3 display the highest REE concentrations associated with a slight deepening of the negative Eu anomaly (Ol-T 2, Yb_N = 10.8–23.9 and Eu/Eu* = 0.5–0.7; Ol-T 3, up to Yb_N = 26.6 and Eu/Eu* = 0.6; Fig. 6d). All clinopyroxenes are distinguished by moderate negative anomalies in Ti and slight depletion in Zr-Hf and Ta relative to neighbor trace elements (Fig. 7c; Zr/Sm = 0.23–0.85 × PM). Strong fractionation relative to neighboring elements is observed for Sr, Pb and Ba on extended trace element patterns (Fig. 7c; Sr/Nd = 0.05–0.48 × PM; Pb/Ce = 0.06–3.7 × PM).

5.3. Geochemical profiles

Rim-to-rim profiles across olivine and clinopyroxene crystals were performed to unravel possible mineral chemical zonation resulting from melt-rock interactions. We excluded small interstitial and isolated grains of clinopyoxene to avoid signature of late stage cooling of trapped melts; thus we selected the largest clinopyroxene grains adjacent to olivine. Results are reported in Fig. 8 for Mg# and trace elements having variable partitioning affinity in olivine (Ni, Mn and Li; Supplementary Material Table S4). For consistency, elements possibly affected by subsolidus re-equilibration were not included in the core-to-rim study as subsolidus re-equilibration takes place first at crystal rims (e.g., Ca and REE; Coogan et al., 2002; Sun and Liang, 2014). For the same reason, we considered only the Ca and REE compositions of cores.

Clinopyroxenes exhibit rather flat profiles in the studied samples, except for some grains that show scattered Mn and Li contents (Fig. 8d–e). This lack of zoning was interpreted as evidence of crystallization in an open system after constant input of undifferentiated melts by Drouin et al. (2009). Olivine also displays flat profiles for all elements considered, except some grains that display scattered Li contents. However, because of serpentinization along olivine edges, all geochemical analyses were performed at a minimum distance of 60 μm from olivine-clinopyroxene contact. As the actual mineral/mineral interface could not be measured, we cannot preclude possible local chemical variations at olivine rims. The possible impact of this gap in data on the shape of geochemical profiles is taken into account in the discussion.

Although element diffusion in olivine is anisotropic (e.g., Dohmen and Chakraborty, 2007), profile along distinct crystallographic axes display comparable compositions and shape in single olivine crystals (Supplementary Material Table S2). For this reason, in Fig. 8, we do not distinguish profiles along the fastest axis [001] from those along [100] and [010], and all analyzed profiles are reported for selected samples.

6. Discussion

6.1. Evidence of reactive olivine-rich troctolites

Textural relationships in Ol-T display deformed olivine grains embayed, sometimes dismembered and partly corroded, against clinopyroxene and/or plagioclase suggesting disequilibrium and reaction between olivine and interstitial phases. Conversely, clinopyroxene and plagioclase show no evidence of deformation and share sharp, relatively planar contacts indicative of equilibrium and crystallization from a common parent melt. Subgrain microstructures observed in olivines from studied Ol-T are similar to those found in some oceanic gabbros, which are interpreted to form at subsolidus condition in lower oceanic crust cumulates (Yoshinobu and Hirth, 2002). However, the strong CPO characterizing these olivine gabbros are in contrast with the weak olivine CPO of Ol-T from the Atlantis Massif (Drouin et al., 2010; this study).

Fig. 7. Primitive mantle-normalized trace element concentration diagrams for a) olivine, b) plagioclase and c) clinopyroxene from Ol-T of IODP Hole U1309D. Symbols and colors refer to the type of Ol-T. Olivines from abyssal peridotites of Gakkel Ridge (D'Errico et al., 2016) are shown for comparison. The grey fields are olivine, plagioclase and clinopyroxene cores in Ol Troctolites of Atlantis Massif from Drouin et al. (2009). Normalizing values after Sun and McDonough (1989).

Mineral chemistry and modal compositions provide complementary lines of evidence against the formation of Ol-T by a simple process of fractional crystallization. The most primitive olivine compositions are found in Ol-T 1 (<75 vol% of olivine), whereas Ol-T 2 (>75 vol% of olivine) have olivine compositions similar to those of Hole U1309D olivine gabbros (Drouin et al., 2009, 2010; Miller et al., 2009) containing 5 to 45 vol% olivine, 40 vol% plagioclase and 15 to 55 vol% clinopyroxene. Ol-T 3, which was sampled near gabbroic veins, displays the most evolved olivine compositions, although these compositions still overlap those of Ol-T 1 and 2, independently of olivine contents. So, the chemical and modal variations of olivine are inversely correlated, in opposition to what is expected for a simple crystallization and magma differentiation trend (Villiger et al., 2007; Fig. 5). Also, olivines show a wide range of Ni and Li contents at a given olivine Mg# (Fig. 5); such trends are not predicted by models of magmatic crystallization. Ol-T 1, which have the most primitive compositions, have also significantly more clinopyroxene (up to 25–30 vol%, Table 1) than the others Ol-T and associated olivine gabbros, further suggesting an atypical differentiation trend. Clinopyroxene is characterized by high Mg#, which is classically interpreted as indicating high pressure crystallization (between 5 and 10 kbar; e.g., Grove et al., 1992), but this interpretation is however inconsistent with the low pressure conditions envisaged for the building of the gabbroic sequence at the Atlantis Massif OCC (Drouin et al., 2009; Grimes et al., 2008). Cores of large clinopyroxene crystals are characterized by a lack of (or small) Eu negative anomalies indicating early precipitation before or simultaneously with plagioclase, in contrast to the expected fractional crystallization trends of MORB-type melt that predict early plagioclase crystallization (e.g., Grove et al., 1992; Villiger et al., 2007). Yet, in all Ol-T, trace element contents of clinopyroxene and plagioclase are in equilibrium with MORB-type melts (Drouin et al., 2009), indicating that they crystallized after a relatively evolved melt having compositions similar to those of basalts from Site U1309 (Mg# ~ 57, Godard et al., 2009; Fig. 6 in Drouin et al., 2009). In contrast, Mg# of melts calculated from clinopyroxene-olivine pairs show more primitive compositions (Mg# = 58–66; Fig. 9).

Finally, the enrichments in the most incompatible elements in olivines (i.e., U and HFSE) from Hole U1309D Ol-T seem to complement the strong depletion in selective elements (i.e., Zr-Hf) in plagioclase. This suggests re-equilibration of olivine with locally enriched MORB-type melts by the relatively 'instantaneous' crystallization of plagioclase and clinopyroxene. In contrast, disequilibrium signatures are observed for other incompatible elements (e.g., REE; Fig. 6 in Drouin et al., 2009) suggesting that re-equilibration may be not achieved for all elements. On the basis of Zr-Hf positive anomalies and enrichments in other incompatible elements in olivine, similar conclusions have been reported by recent geochemical studies on Ol-T from the Alpine ophiolites (Basch et al., 2018; Rampone et al., 2016; Sanfilippo et al., 2014). Rampone et al. (2016) recently proposed that concomitant processes of olivine assimilation and plagioclase crystallization at decreasing melt mass are the mechanisms controlling HFSE anomalies in olivine and adjacent phases.

Combined textural, microstructural and chemical characteristics of U1309D Ol-T indicate that they formed after a reactive process of olivine assimilation and concomitant crystallization of interstitial plagioclase and clinopyroxene. This melt-rock interaction progressively decreases olivine modal contents, and may accounts for an increase in MgO and Ni contents of the migrating melt (e.g., Collier and Kelemen, 2010; Lissenberg and Dick, 2008), while local crystallization of interstitial phases increases its contents in strongly incompatible elements. Modeling of the reactive process generally assumes that a MORB-type melt infiltrates and partially dissolves a pre-existing olivine matrix and recrystallizes new olivine, new plagioclase and additional clinopyroxene (e.g., Lissenberg and Dick, 2008; Rampone et al., 2016; Sanfilippo et al., 2014). Crystallization of clinopyroxene and plagioclase is generally thought to be preceded by formation of dunites with abundant crystallization of new crystals of olivine (e.g., Kelemen et al., 1997).

Assimilation-Fractional Crystallization (AFC; DePaolo, 1981) is the most common and largely used model to reproduce chemical and modal variations at constant thermodynamic parameters. AFC models have been used to simulate the variations of major elements only (e.g., Lissenberg and Dick, 2008) or of minor and of some trace elements (i.e., Ti, Y, Zr, Hf; Rampone et al., 2016; Sanfilippo et al., 2014) during melt-rock interactions. The trends shown by other elements, in particular REE, were not reproduced successfully by this approach thus suggesting that element mineral-melt exchange is not the only control on Ol-T and MORB compositions in a reactive system. These trends may be controlled also by element transport by migrating melts, which can play an important role in the re-distribution of the most incompatible elements (chromatographic effect, Navon and Stolper, 1987).

In the following sections, we first simulate melt-rock interactions by geochemical numerical modeling to quantify the effect of reactive transport through a porous media on the chemistry of reactive Ol-T. Then, we investigate the equilibrium signature of mineral phases forming the U1309D Ol-T.

6.2. Numerical simulations of compositional variations

6.2.1. Model setup

The reaction process described above is triggered by a melt that infiltrates in an olivine-rich porous medium and thus controls element transport through the crystal matrix. In turn, melt flow through a solid matrix is governed by the 'percolation threshold' (fraction of melt produced > total porosity, Turcotte and Morgan, 1992). At constant melt viscosity, the percolation threshold is controlled by porosity (melt volume fraction), connected porosity and permeability (e.g., Kelemen et al., 1997; Turcotte and Morgan, 1992). Accordingly, the pre-existing porosity and permeability may be an important additional factor in determining melt composition and behavior during the reactive process. The formation of the most primitive Ol-T 1, which display the highest clinopyroxene and plagioclase modes compared to Ol-T 2 with <25 vol% of interstitial phases, could be related to a higher percolation threshold leading to higher melt/rock ratios.

The initial composition of the olivine-rich porous medium is set as that of a mantle harzburgite based on the following arguments. The heterogeneous plutonic section at the Atlantis Massif lacks the typical well-developed modal layering generally described in settings where cumulate-derived Ol-Ts form (e.g., Bédard, 2015; Holness et al., 2007). The latter originate during the construction of a cumulate differentiation series in metres thick lenses ('intra-crustal origin', Renna et al., 2016) or in large magma chambers (e.g., Bédard et al., 2000; Bédard, 2015; O'Driscoll et al., 2007). In contrast, there is no structural evidence for magma chambers in Hole U1309D (e.g., Blackman et al., 2011; Grimes et al., 2008), and geochemical data does not indicate that the downhole gabbroic series formed by a continous magma fractonation process (Fig. 2). Also, dunitic cumulates are not described in Hole U1309D. Dunitic cumulates would contain olivine with similar Mg# and REE contents compared to those of a mantle dunite, but higher Ni contents (see Supplementary Material). These features, together with the microstructural constrains from Drouin et al. (2010) lead us to discard the hypothesis of cumulate precursor of Ol-T from the Atlantis Massif. The Ni concentrations in olivine from the studied Ol-Ts are higher than those in associated troctolites and olivine gabbros, but are comparable to olivines from abyssal peridotites (Fig. 10c). We hypothesize that the impregnated harzburgites intruded by the plutonic sequence observed in the shallowest 200 m at Site U1309 (Tamura et al., 2008) preserved the first stages of melt impregnation of the shallow mantle prior to the extensive melt percolation that formed Ol-Ts.

We model the evolution of Ol-T from a harzburgitic matrix using a reactive porous flow numerical model, the 'Plate Model' proposed by Vernières et al. (1997) for REE contents and modified by Bedini et al. (2002) for Mg# contents, to explore the chemical effect on relict minerals and melt compositions. This model allows simulations in a rock-
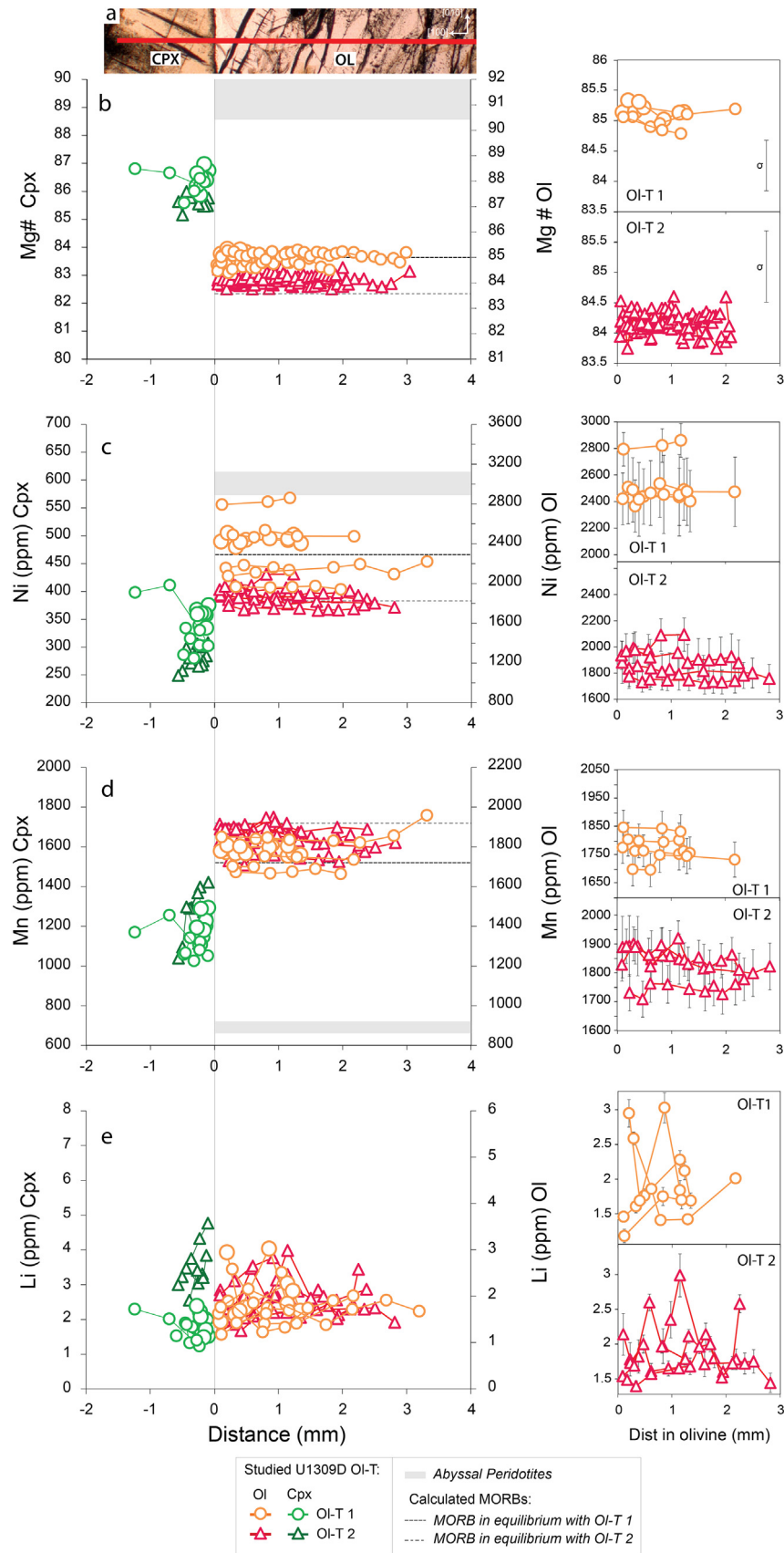
Fig. 8. Chemical profiles across olivine and neighboring clinopyroxene. Profiles were performed along one of the principal axes of olivine ([100], [010], or [001]; see Analytical methods for further details) as illustrated in a) CPX = clinopyroxene, OL = olivine. Similar compositions were observed along different axes, and therefore no axis-distinction is made. We report a selection of two Ol-T1 (305-U1309D-248R-2W, 38–41; 305-U1309D-248R-2W, 43–48) and two samples of Ol-T2 (305-U1309D-247R-3W, 16–18; 305-U1309D-248R-3W, 36–38) for the following elements: b) Mg#, c) Ni (ppm), d) Mn (ppm), e) Li (ppm). Olivine profiles from single samples are enlarged on the right side of the figure. For comparison we report data of olivines from abyssal peridotites (De Hoog et al., 2010; D'Errico et al., 2016) and calculated olivine compositions in equilibrium with neighboring clinopyroxene (see text for details).
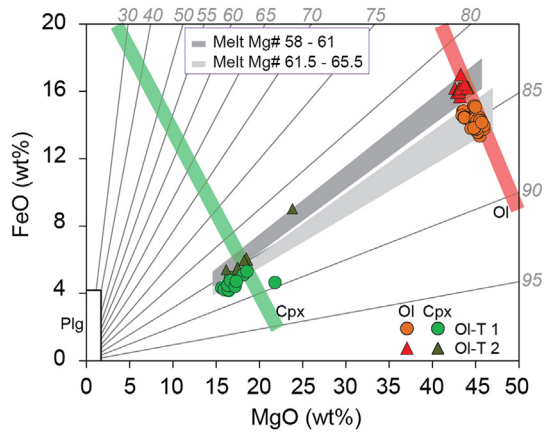
Fig. 9. MgO (wt%) versus FeO (wt%) in olivine (red and orange symbols), and clinopyroxene (green symbols). Grey fields show the calculated range of compositions of olivine and clinopyroxene from melts in equilibrium with measured minerals. Calculations were performed using Petrolog3 (see Fig. 5 for details on the model) by selecting melts in equilibrium with measured clinopyroxene-olivine couples. Thin grey lines indicate iso-Mg# lines for Mg# ranging from 30 to 95. Variations of MgO and FeO are represented for olivine (Ol) in red line, clinopyroxene (Cpx) in green line and plagioclase (Plg) in white box.

dominated system where the solid matrix buffers the melt composition. We simulate an open system and multi-stage process to reproduce the formation of compositional variations at centimeter scale observed in Hole U1309D Ol-T. Two main stages are modeled. *Stage 1* is the dunitization process that reproduces complete dissolution of pyroxenes in the starting harzburgite by an incoming melt assuming the following reaction:

$$pyroxenes + melt_{in} = olivine_p + melt_{Si}$$
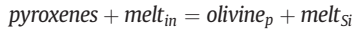
where 'pyroxenes' are mantle orthopyroxenes and clinopyroxenes, 'melt$_{in}$' is the infiltrating (=incoming) Primary MORB, 'olivine$_p$' is the olivine precipitated at the rims of the mantle olivine (Saper and Liang, 2014), and 'melt$_{Si}$' is the Si-saturated melt resulting from the reaction.

Stage 2 simulates olivine assimilation (hereafter referred to as M$_a$ = assimilated mass/infiltrating melt mass; see Supplementary Material) and progressive evolution of the infiltrating melt by crystallization of plagioclase and clinopyroxene following the reaction:

$$olivine_m (+olivine_p) + melt_{in+Si} = olivine_2 + clinopyroxene + plagioclase + melt_r$$
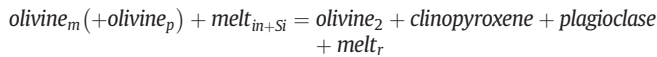
here, 'olivine$_m$' is the pre-existing mantle olivine partially modified by *Stage 1* (olivine$_p$); 'melt$_{in+Si}$' is the reacting melt composed of Si-rich melts after *Stage 1* and inputs of Primary MORB melt in an open system; 'olivine$_2$' represents the remaining olivine after reaction, re-equilibrated with the residual (='reacted') 'melt$_r$'. We applied this approach to similate Fe-Mg exchanges (referred to as Mg# model in this study), chemical variations of Ni in olivine (Ni model), and REE contents in olivine (REE Plate model) during the formation of Ol-Ts. To evaluate the effect of simultaneous precipitation of plagioclase and clinopyroxene, we combined the results of the Mg# model with modal plagioclase variations during simple fractional crystallization (hereafter referred to as Combined model, Fig. 10).

Variations of Ni contents in olivine were calculated after the modified melt at each reaction increment from the Mg# model assuming:

$$C_{TOT}^{Ni} = \phi C_L^{Ni} + (1-\phi) C_S^{Ni}$$

where the total concentration of nickel in the reactive cell, C_{TOT}^{Ni}, is expressed by Ni concentration in the interstitial melt, C_L^{Ni}, and in the

solid material, C_S^{Ni}. Here, ϕ is the porosity and, for simplicity, we assume similar density for all phases. Knowing $C_S^{Ni} = D_G^{Ni} C_L^{Ni}$ (D_G^{Ni} = bulk partition coefficient of Ni), the equation of C_{TOT}^{Ni} can be solved for C_L^{Ni} at each reaction increment "i":

$$C_{L_i}^{Ni} = \left(C_{TOT}^{Ni} - \phi_i\, C_{L_{i-1}}^{Ni} \right) / (1 - \phi_i)\, D_{G_i}$$

Based on the dependence of nickel partitioning on melt composition, we obtained equilibrium olivine using the Ni partition coefficient calculated at each reaction increment as function of MgO in the melt (equation after Hart and Davis, 1978).

We compared our models to the commonly used melt-dominated numerical models. We simulated the reaction of *Stage 2* with the AFC model for REE. Also, we reproduced trends of fractional and in situ crystallization to test the possible contribution of magmatic crystallization in the formation of chemical variations of Ol-T.

Following the calculated crystallization temperatures of plagioclase (~1230 °C; Drouin et al., 2009) and estimated pressure at which the gabbroic sequence at the Atlantis Massif formed (~7 km; Grimes et al., 2008), we used mineral/melt partition coefficients obtained at temperature in the range 1100–1200 °C and pressure of about 2 kbar. For *Stage 1* we used the whole rock composition of harzburgite from ODP Hole 1274A (Godard et al., 2008) as proxy for the mantle precursor of Hole U1309D Ol-T. Single phase compositions were taken from harzburgite collected at the Gakkel Ridge (D'Errico et al., 2016), which have mineral modal and calculated bulk rock compositions comparable to Hole 1274A harzburgite. Starting composition for *Stage 2* are the reacted and modified whole rock compositions after reaction in *Stage 1*. Due to the chemically heterogeneous feature of mantle relicts recovered at the Atlantis Massif (Miller et al., 2009; Tamura et al., 2008), two representative impregnated harzburgites were selected within IODP Hole U1309D for Ni simulations: from depths of 133 (H1; Tamura et al., 2008) and 173 mbsf (H2; Miller et al., 2009). For the Primary MORB magma ('melt$_{in}$') we used the estimated composition of melt formed by 6% aggregated fractional melting of a Depleted MORB Mantle (Workman and Hart, 2005). Only for simulations of REE we used a relatively more evolved melt (Gale et al., 2013) as a proxy of the last impregnation event recorded by Ol-T. Rock and melt starting compositions are reported in Supplementary Material Table S6, and partition coefficients used are in Supplementary Material Table S4. Further details on the Plate Model used in this study are given in the Supplementary Material - analytical methods and models.

6.2.2. Mg#-Ni simulations

The Mg# and Ni simulation of *Stage 1* produces only a slight decrease in olivine Mg# down to ~91 with invariable Ni contents (Fig. 10a), at relatively constant porosity. *Stage 2* produces significant decrease in olivine Mg# (down to 83.5) at variable extents of olivine dissolution (ol vol% = ol%/(cpx% + ol%)). At low M$_a$ (0.01–0.02) the effect of the reaction is to decrease olivine Mg# at relatively constant modal contents, whereas higher M$_a$ (between 0.06 and 0.13) accounts for a decrease in modal olivine at comparable but modest Mg# variations (Fig. 10a). The lowest olivine Mg# of the most olivine-rich Ol-T 2 (and Ol-T 3) are reproduced by low M$_a$ in comparison with olivine in Ol-T 1 that is produced by higher olivine assimilation at higher proportion of interstitial melt. This confirms that pre-existing porosity and permeability, controlling the melt/rock ratio, play a fundamental role in the reactive process. However, this model does not reproduce the entire range of olivine modal contents of Ol-T 1, suggesting that other processes must be invoked, such as crystallization of the interstitial melt. The Combined model (Fig. 10b) reproduces all olivines in Ol-T 1 suggesting that their compositions result from melt-rock interactions at increasing melt mass and abundant precipitation of interstitial phases. We note, however, that the Combined model does not reproduce the modal content of Ol-T 2 and Ol-T 3. This is probably related to an over-estimation of
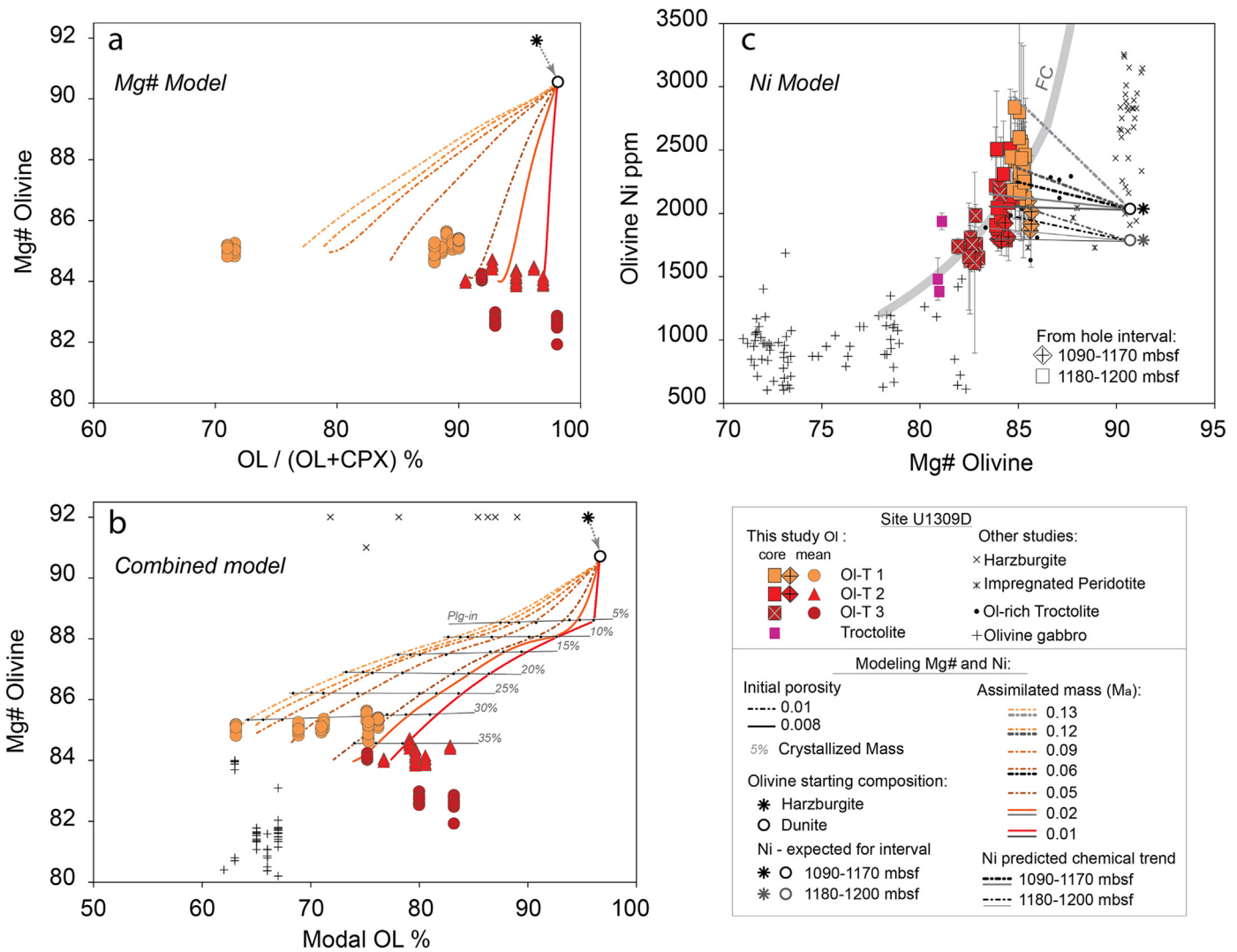
Fig. 10. Mg# (=100 × Mg/(Mg + Fe)) versus a) modal olivine [ol/(ol + cpx)] and b) total modal olivine [ol/(ol + plg + cpx)] for Hole U1309D Ol-T. c) Mg# versus Ni contents in olivine. Olivines from abyssal harzburgite (D'Errico et al., 2016) and Hole U1309D olivine gabbro, olivine-rich troctolites, and impregnated harzburgites (Drouin et al., 2009; Miller et al., 2009; Suhr et al., 2008) are also reported for comparison. Data from this study are compared with reactive percolation modeling of a) Mg# model, b) Combined model, c) Ni model. Numerical experiments of melt-rock interactions were performed with the "Plate Model" of Vernières et al. (1997), initially designed for trace element applications (see text for details on the model). In c) two compositions of olivine in impregnated harzburgite were used as expected starting material for formation of Ol-T from intervals 1090–1170 mbsf and 1180–1200 mbsf, respectively with the maximum Ni contents (U1309D-31R-2, 46–48 cm, 173 mbsf, Ni = 2000 ppm) and minimum Ni (U1309D-23R-2, 8–13 cm, 133 mbsf, Ni = 1750 ppm). Initial conditions of models and all other starting material compositions are reported in the text and in Supplementary Material Table S4 and S6. Two stages of melt-rock interactions are modeled (see text for details on reactions). *Stage 1* (light grey arrow) form dunite that was used as starting material for *Stage 2*. Reaction in *Stage 2* simulates percolation of an N-MORB sequentially more evolved at decreasing melt mass (%, reported in italic) by crystallization of clinopyroxene (and plagioclase). We used a simplified multi-stage approach whereby successively evolving melts infiltrated and reacted with the protolith. The latter is the resulting solid matrix from each previous reaction increment. The results of *Stage 2* are shown in red to orange lines in a) and b), and black to grey lines in c) for different values of olivine mass assimilated (0.13 to 0.01, see legend). Fractional crystallization trend (FC, light grey line) was calculated with Petrolog3 (see Fig. 5 for details) and reported in c) for comparison; K_{Ni} vary during simulation following Beattie et al. (1991).

plagioclase crystallization during the formation of Ol-T 2 and Ol-T 3 where dissolution and precipitation are minor processes.

Nickel simulations of *Stage 2* presented in Fig. 10c indicate that Ni contents of olivine in Ol-T from interval 1090–1170 mbsf (Ni = 1790–2018 ppm) may be accounted for by reactive melt percolation through H1 (harzburgite at 133 mbsf in Hole U1309D). The same process may explain the origin of Ol-T collected between 1180 and 1200 mbsf from mantle protolith H2 (harzburgite at 173 mbsf in Hole U1309D). Thus olivine in the studied Ol-T inherits Ni concentrations from olivine in their mantle precursors. We note however that olivine has a wide range of Ni contents in the deeper interval of Ol-T (Fig. 10c). The highest Ni are obtained by models run at high M$_a$ (up to 0.13), in contrast with low M$_a$ (0.01–0.06) that produce no variation or solely a small increase in Ni contents. This suggests that the more reactive is the system (hence more Ni available in the percolating melt), the more variable are olivine compositions (e.g., Ol-T 1).

To summarize, Fe-Mg and Ni contents remain relatively constant during dunitization in *Stage 1* (e.g., Kelemen et al., 1997), and variable compositions at centimeter scale are formed after *Stage 2* of the reactive process. Ol-T 1 is the most reactive type of Ol-T, which is also affected by abundant crystallization of interstitial clinopyroxene and plagioclase in equal proportions (cpx/plg ~ 1). In contrast, the composition of olivine in Ol-T 2 and Ol-T 3 is "buffered" by a slightly modified percolating melt. These local heterogeneities in Ol-T are likely inherited from the mineral modal distribution of the pre-existing harzburgitic matrix (i.e., orthopyroxene/olivine ratio), which in turn controls permeability and governs the melt/rock ratio of the system (e.g., Kelemen et al., 1997; von Bargen and Waff, 1986). Moreover, the measured and

modeled strong variability of Ni contents in olivine demonstrate that not only reaction and crystallization have an effect on Ol-T formation, but locally olivine compositions also partially inherit those of the pre-cursor mantle harzburgite.

6.2.3. REE models

In contrast to constraints from Mg# and Ni modeling, results of the REE Plate model show that *Stage 1* produces olivine with higher REE and less fractionated pattern ($Yb_N = 0.6$; $Dy_N/Yb_N = 0.18$) than the initial mantle olivine (Fig. 11). Olivine$_p$ (see reaction *Stage 1* above) is in equilibrium with melt that is progressively saturated in silica and enriched in incompatible elements. Numerical simulations of *Stage 2* using the REE Plate model reproduce olivine with lower MREE to HREE fractionation at lower M_a (0.08–0.1) compared to models at greater M_a (0.19), but variations are small and negligible within the compositional interval of Ol-T from this study (Fig. 11). Curves reproduced for different clinopyroxene/plagioclase ratios also show negligible or little effect on REE contents in olivine.

AFC models of *Stage 2* can account for strong REE fractionations but the modeled REE abundances do not fall in the range of compositions of olivines from U1309D Ol-T (Fig. 11), suggesting that melt composition does not represent the principal factor controlling chemical variations in U1309D Ol-T. The simulated trends of fractional crystallization and

Fig. 11. Ratio Dy_N/Yb_N versus Yb_N (N = normalized to Chondrites; Sun and McDonough, 1989) in olivine cores from Ol-T 1 and Ol-T 2. Data are compared with modeling of REE variations in olivine during fractional melting (FM), magmatic crystallization (in situ and fractional crystallization), Assimilation-Fractional Crystallization (AFC) and reactive percolation ("Plate Model", thick lines). Chemical trend of fractional melting was estimated with the equation proposed by Johnson et al. (1990) using the parameterization of Kinzler (1997). The starting material is a depleted harzburgite from ODP Hole 1272A (Godard et al., 2008). Magmatic crystallization was modeled using the equation proposed by Langmuir (1989) where 'f' is the fraction of melt that returns to the magma chamber after its partial crystallization (f = 1 simulates fractional crystallization). Curves were obtained for increments of crystallized mass of 2%. Olivine compositions were computed by AFC model (DePaolo, 1981) at decreasing melt mass (F = 0.95–0.10). The model assumes that initial melt assimilate olivine (M_a = 100% olivine) and crystallize plagioclase + clinopyroxene in different proportions (cpx/plg = 1 and cpx/plg < 1). REE variations were predicted using the 'Plate Model' of Vernières et al. (1997) in an open system (see text for details on reactions). Reaction *Stage 1* (thick light grey arrow) form dunite that was used as starting material for *Stage 2*. Results from *Stage 2* (thick curves) were performed at different olivine dissolution rates (M_a is the proportion of dissolved olivine in each simulation). Reported values in italic indicate the proportion of assimilated and crystallized fraction (M_a/M_c) at each reaction increment. K_d used for crystallization, melting and melt-rock interaction models are reported in Supplementary Material Table S4, and starting compositions in Supplementary Material Table S6.

in situ crystallization plot towards less fractionated REE and higher Yb_N, in contrast with depleted olivines in Ol-T (Fig. 11).

The olivine compositions simulated with the REE Plate model best reproduce those of U1309D Ol-T, in comparison with AFC and other melt-dominated models. However, measured and simulated Dy_N/Yb_N of olivines have similar, although scattered, REE contents in Ol-T 1, 2 and 3. This suggests that melt-rock reaction is not the unique control on chemical compositions and formation of Ol-T, and that dissolution of olivine has little effect on trace element composition of the migrating melt. Thus, REE Plate models demonstrate that melt transport is an additional factor driving element re-partitioning in a reactive percolation system. During melt transport and melt-rock interactions, MREE move faster and tend to be 'buffered' by percolating melts while the relatively slower HREE are governed by local changes in solid compositions and therefore decrease steadily (Godard et al., 1995; Navon and Stolper, 1987; Vernières et al., 1997); as a consequence, strongly fractionated REE patterns in olivine are produced (Fig. 11).

REE modeling, together with Mg# and Ni simulations, demonstrate that Ol-Ts inherit mantle Ni heterogeneities, and their formation is affected by mineral modal distribution of the harzburgitic matrix. In particular, modeling of Ni and REE Plate model indicates that the composition of pre-existing solid matrix exert a strong control on melt-rock reaction and compositional variations at the local scale between Ol-T 1 and 2, which points to a rock-dominated system.

6.3. Chemical equilibrium in U1309D olivine-rich troctolites

Chemical equilibrium between phases is described by element mineral/melt partition coefficients (e.g., Bédard, 2005). Partitioning depends on pressure, temperature and melt composition (e.g., Hart and Davis, 1978; see Supplementary Material Table S4) and, therefore, it may vary during melt-rock interactions (especially Ni, e.g., Hart and Davis, 1978). Experimental studies have shown that, upon melt-rock interactions, element abundances at rims of pre-existing minerals (such as olivine) are locally modified to reach instantaneous equilibrium with the percolating melt (e.g., Lambart et al., 2009; Liang, 2003; Van den Bleeken et al., 2011). This effect results in core-to-rim compositional variations within crystals.

In contrast to these findings, clinopyroxene-to-olivine profiles in U1309D Ol-Ts show that for all analysed elements no core-to-rim variations are preserved. Element diffusion governs the intra-crystal composition after local rim modification (e.g., Chakraborty, 2008; Liang, 2003). Hence, slower element diffusion rates (Supplementary Material Table S5) compared to olivine dissolution rates (10^{-16}–10^{-20} m²/s, Kvassnes and Grove, 2008) may prevent re-equilibration of olivine rim within a minimum distance from the melt-crystal boundary (i.e., compression of diffusion profile by dissolution, Liang, 2003). In this scenario, olivine would preserve its original core composition distinguished by high Mg# and low Mn contents similar to the associated harzburgite or common dunitic cumulates, which is not the case of olivines in Ol-T from Atlantis Massif (Figs. 5 and 8). Also, for some elements (i.e., Fe-Mg, Ni and Li, Supplementary Material Table S5) diffusion rates in olivine are slightly higher than dissolution rates, indicating that not all elements should present a flat profile in olivine.

An alternative hypothesis is that olivine flat profiles could represent the evidence of relatively fast element transport by intra-crystalline diffusion. At high temperatures, as those calculated for plagioclase crystallization in Hole U1309D Ol-Ts (~1230 °C; Drouin et al., 2009), element diffusion becomes more efficient (Chakraborty, 2008, and references therein), and olivine crystal composition may be completely modified. The lack of chemical variations between profiles along different preferred crystallographic directions in single olivine further suggests a compositional reset of olivine, operated by element diffusion. In this model, interstitial phases crystallized after the modified melt have to be in equilibrium with olivine. To test this hypothesis, we
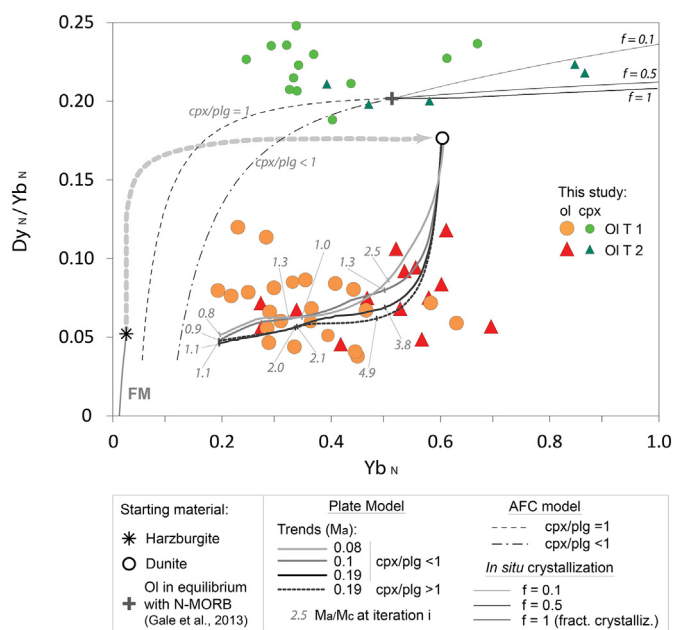
calculated melts in equilibrium with olivine and adjacent clinopyroxene for the most relevant elements.

We selected mineral-melt partition coefficients (Supplementary Material Table S4) experimentally determined at conditions that best match those predicted for the formation of the gabbroic sequence at the Atlantis Massif: T = 1100–1200 °C (Drouin et al., 2009) and P = 2 kbar (Grimes et al., 2008). In order to account for MgO-melt and mineral-stoichiometry control on partitioning of compatible and moderately incompatible elements in olivine (e.g., Hart and Davis, 1978), we used fractional crystallization modeling (in this study Petrolog3; Danyushevsky and Plechov, 2011) that calculate mineral and melt compositions as function of varying partition coefficients (Fig. 9). Partitioning of incompatible elements is Si-melt dependent (e.g., Evans et al., 2008). Dissolution-precipitation processes at Site U1309 change mainly the melt MgO contents, whereas silica variations are negligible. Hence, the simple $C_L = C_s / {}^{S-L}K_d$ (C = element content in L, melt and S, solid; K_d = element partition coefficient) was applied. For REE, we used mineral/melt partition coefficients derived from measured olivine and clinopyroxene compositions according to a recently developed lattice strain model (Sun and Liang, 2014), using the approach of Rampone et al. (2016).

Our calculations show that chemical equilibrium between olivine and clinopyroxene is observed for major and minor elements mainly hosted by olivine in primitive rocks (De Hoog et al., 2010), namely Fe-Mg, Ni and Mn (Figs. 8 and 9), and for Li, a trace element concentrated in olivine (${}^{Ol/Melt}K_{Li} \geq {}^{Plg/Melt}K_{Li} > {}^{Cpx/Melt}K_{Li} > {}^{Opx/Melt}K_{Li}$, Supplementary Material Table S4). In primitive rocks, other trace elements such as REE are hosted by clinopyroxene (${}^{Cpx/Melt}K_{REE} \geq {}^{Opx/Melt}K_{REE} > {}^{Plg/Melt}K_{REE} > {}^{Ol/Melt}K_{REE}$, Supplementary Material Table S4): the melts computed from the new dataset of REE contents display comparable HREE (Yb in particular) in all phases, whereas the strong MREE to LREE depletion in melts computed in equilibrium with olivine (Drouin et al., 2009) is still observed.

Finally, computed melts in equilibrium with clinopyroxene-olivine couples have higher Mg# of 62–66 for Ol-T 1 compared to melt Mg# of 58–61 found for Ol-T 2 (Fig. 9), which is consistent with the shift of MORB-type melts towards more primitive compositions after assimilation of olivine (Lissenberg and Dick, 2008). Re-equilibration times are evaluated, further in the discussion, to constrain the control of diffusion mechanism on mineral geochemical composition.

6.4. Genesis of olivine-rich troctolites at Atlantis Massif

The results of analyses and modeling presented above are consistent with the formation of Ol-T recovered at the Atlantis Massif OCC after intensive melt impregnation of a depleted mantle harzburgite through a multi-stage reactive percolation process. Relicts of the pre-existing matrix can be recognized in the upper 200 m of IODP Holes U1309B and U1309D (Blackman et al., 2011; Tamura et al., 2008). The migration of a primary olivine-saturated MORB-type melt lead to concomitant mantle pyroxenes dissolution and olivine precipitation around the original mantle olivine (Liang, 2003; Saper and Liang, 2014), thereby generating undersaturated olivine melts. The extent of melt-rock interactions is locally controlled by the orthopyroxene distribution in the harzburgitic protolith. The crystallization of <8% of total melt (after modeling with Petrolog3) in new olivine crystals drove the percolating melt towards Si-rich compositions, thus suggesting that rather pervasive melt-mantle interactions (Collier and Kelemen, 2010) can account for the formation of Ol-T. If this is the case, melt migration through grain-scale porous flow, and the formation of Ol-T, took place in the transition from melting to crystallization region (e.g., Collier and Kelemen, 2010) beneath the Mid-Atlantic Ridge at the Atlantis Massif.

We propose the following scenario for the formation of Ol-Ts drilled at the Atlantis Massif (Fig. 12).

(i) The upwelling heterogeneous depleted mantle records partial melting episodes leaving behind harzburgites with variable
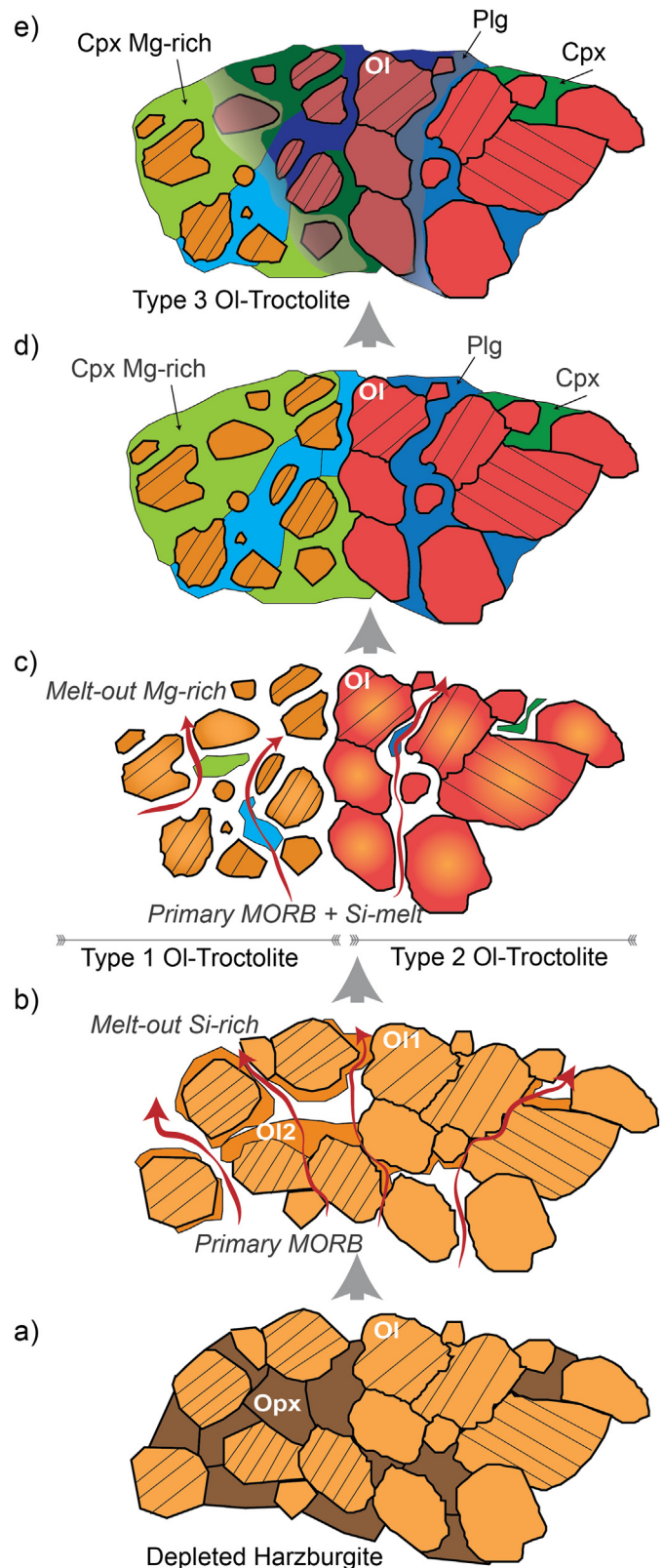

Fig. 12. Schematic representation of sequential processes of melt impregnation forming Ol-T drilled at the Atlantis Massif. Percolation of primary MORBs through a heterogeneous residual harzburgite (from a) to b)) dissolve primary orthopyroxenes and crystallize olivine at rims of mantle olivine. Areas where higher proportions of orthopyroxene were originally present lead to higher porous flow and more production of Si-melt that dissolve olivine and form Ol-T 1 (from c) to d) on the left) with high Mg# clinopyroxene. Zones of higher initial permeability form Ol-T2 at less olivine assimilation extents (from c) to d) on the right). More evolved reacted melts crystallize at decreasing temperature in cross-cutting gabbroic veins forming Ol-T 3 (e).

compositions and (ortho)pyroxene modal contents (Fig. 12a), which constitute the lithospheric oceanic mantle. At shallow levels, primary MORB-type melts sporadically migrate upwards, forming gabbroic veins and dykes, and reactive porous flow locally occurs in the infiltrated mantle lithosphere. This event of melt impregnation occurs at low melt/rock ratios (Tamura et al., 2008).

(ii) Further inputs of primitive MORBs trigger dissolution of orthopyroxene and melt influx becomes a dominant process. Simultaneously, new olivine crystallizes at the rims of mantle olivine (Fig. 12b) decreasing the melt MgO (e.g., Lambart et al., 2009; Saper and Liang, 2014). Orthopyroxene-rich zones of the mantle precursor have initially the lowest permeability (Toramaru and Fujii, 1986), and therefore form local permeability barriers where melt tend to accumulate. In turns, the significant volume of melt accumulated favors assimilation of mantle pyroxene (e.g., Pec et al., 2017), and locally enhances permeability. On the other hand, local orthopyroxene-poor zones have higher permeability that favors migration of the melt, leading to lower assimilation of mantle pyroxene. The progressive dissolution of orthopyroxene increases the Si contents of the percolating MORB, as well as its Cr concentrations (e.g., Arai et al., 1997). The pre-existing olivine fabric is disrupted and olivine CPO's with [001] cluster develop at high melt/rock ratios (≥30% melt, Drouin et al., 2010). The migrating melts become silica-saturated and the original harzburgite is transformed in an olivine + Si-melt system (e.g., Lambart et al., 2009).

(iii) At this stage, the silica-saturated melt and the dunitic matrix are in disequilibrium, and olivines tend to be partially dissolved (=assimilated). As reaction progress, local distinct Ol-Ts form. Higher dissolution of mantle orthopyroxene produces more Si-saturated melt leading to higher olivine assimilation (Fig. 12c). The latter accounts for the increase in MgO of the modified percolating melts and triggers the early crystallization of high Mg# poikilitic clinopyroxene in the most reactive Ol-T 1 (Fig. 12d). Zones with lower modal orthopyroxene lead to lower Si-melt production and record less olivine dissolution and minor crystallization of high Mg# clinopyroxene over plagioclase (cpx/plg ≪1). Olivine re-equilibrates with a progressively evolved melt by crystallization of interstitial phases forming Ol-T 2 (Fig. 12d). Cr from the orthopyroxene-melt reaction is hosted in interstitial clinopyroxene, as evidenced by its high Cr contents (Cr_2O_3 is up to 1.5 wt% in Ol-T, Drouin et al., 2009 and this study; Cr_2O_3 ~1.2 wt% in primitive oceanic gabbros, e.g., Ross and Elthon, 1997).

(iv) Relatively more evolved reacted MORB-type melts crystallize at decreasing temperature in cross-cutting gabbroic veins that 'buffer' the composition of pre-existing Ol-Ts and form Ol-T 3 (Fig. 12e).

6.5. The geodynamic context of Olivine-rich troctolites

The lower oceanic crust drilled at the Atlantis Massif was built by multiple injections of MORB-type melts in the absence of a steady-state magma chamber (Blackman et al., 2011; Godard et al., 2009; Ildefonse et al., 2014). The uppermost section of Hole U1309D is younger than underlying intrusive series, which implies that the intrusive activity occurred at different depths below the mid-ocean ridge during low angle rotation of the detachment fault (Grimes et al., 2008). Data from this study show that Ol-T formed after mantle rocks. Ol-Ts result from a period of enhanced magmatism at depth, as already proposed for the Atlantis Massif (Blackman et al., 2011; Ildefonse et al., 2007) when melt migrated through a harzburgitic mantle by porous flow. This occurred probably during the early formation of the Atlantis Massif OCC (e.g., Blackman et al., 2011; Ildefonse et al., 2007, 2014). We posit that while the magmatic lower oceanic crust formed, shallower mantle screens were preserved due to the decrease in melt supply during

Table 2
Re-equilibration times calculated for Fe-Mg, Mn and Sm. See text for references of reported diffusion coefficients (log D).

Elements	Log D	Re-equilibration time
Fe-Mg	−16.6	210–300 yr
Mn	−17.2	1.5 ka
Sm	−19.2	105 ka

exposure of the Atlantis Massif by long-lived detachment faulting. This is evidenced by the lack of mantle relicts downhole.

The model we propose is valid only if melt-rock interactions, which are found to modify the mantle units intercalated in the gabbroic sequence, occur within a reasonable time compared to emplacement of the gabbroic sequence. Mineral chemical profiles provide evidence of re-equilibration of the original olivine with the percolating and reacting melt by inter-crystal element diffusion. In order to test whether the diffusion mechanism in olivine is fast enough to reset the composition of precursor olivine, we compare the re-equilibration time of selected elements (Table 2) with the time of emplacement of the Atlantis Massif crustal section. We calculated minimum re-equilibration time (t_{eq}) with a simple but effective approach, using the equation $t_{eq} = r^2/\pi D_i$ (r = core-rim distance; D_i = element 'i' diffusion coefficient; Crank, 1975). Olivine was geometrically approximated to a sphere of radius 3 mm, which corresponds to the core-rim length of the coarser analysed grain. We used diffusion rates experimentally obtained at lower oceanic crustal conditions (~1200 °C, quartz–fayalite-magnetite oxygen buffer, and Fo_{90}, Supplementary Material Table S5). Fast diffusion rates were calculated for Fe-Mg (e.g., Dohmen et al., 2007), followed at lower diffusivities by divalent cations Ni, Co and Mn (Jollands et al., 2016; Supplementary Material Table S5). Diffusion of Li occurs through two different site locations in olivine lattice, which favors its fast diffusion rates (Dohmen et al., 2010). To calculate minimum re-equilibration times, Mn was selected as slow diffuser between divalent cations ($D_{Mn} < D_{Ni} < D_{Co}$; e.g., Jollands et al., 2016; Petry et al., 2004). The minimum time required to re-equilibrate an olivine crystal is about 1.5 ka (D_{Mn} from Petry et al., 2004). Vast discrepancies exist between trace element (REE, Ti, Zr, Hf, etc.) diffusivities with rates that span over several orders of magnitude (see discussions in Jollands et al., 2016). Overall, trace elements diffusion rates are lower than (or very close to) Mn diffusivities. Minimum equilibration time of 105 ka was obtained for MREE (D_{Sm} from Remmert et al., 2008).

The smallest re-equilibration times were obtained for comparison based on Fe-Mg exchanges. The minimum time necessary to re-equilibrate Fe-Mg in olivine (D_{Fe-Mg} from Dohmen et al., 2007) is 300 yr. We calculated Fe-Mg diffusivities as a function of Fo content in olivine (using the equation of Dohmen and Chakraborty, 2007) to test the validity of our simplistic method. Olivine initial composition was set at Fo_{90} and its rim at Fo_{84} to simulate re-equilibration in olivine from Ol-T 2. Following this method, Fe-Mg in olivine re-equilibrates in <210 yr showing our method is a relatively good approximation. The discrepancy may relate to differences in Fo content, inversely related to diffusion coefficients (the decrease in Fo increases element diffusion, Dohmen and Chakraborty, 2007) and was kept constant in the first equation.

The calculated melt-olivine re-equilibration times fall in a range below the 200 ka predicted for emplacement of the gabbroic sequence, thus supporting our model whereby Ol-T formed after enhanced melt impregnation of a mantle precursor before, or simultaneously, the building of the lower oceanic crust at the Atlantis Massif.

6.6. The effect of olivine assimilation on MORB compositions

Melt-rock interactions are found to modify MORB compositions by post-cumulus reactions (e.g., Ross and Elthon, 1997), or reactive crystallization through mantle matrix (Collier and Kelemen, 2010) and assimilation of a lower oceanic crust component (Lissenberg and Dick, 2008). The assimilation of a cumulate anorthitic and forsteritic assemblage can shift

MORBs compositions towards apparent higher pressures (Lissenberg and Dick, 2008), as a consequence of the similarity with chemical trends typical of high pressure fractionations (e.g., Grove et al., 1992). In contrast, assimilation of a mantle component, as modeled by steady-state reactive crystallization process, leads to MORB fractionation characterized by constant Mg# at decreasing Ca# (Collier and Kelemen, 2010). Here, we calculate compositions of migrating MORBs after different magnitudes of dissolved mantle olivine in order to quantify how much mantle was assimilated at the Atlantis Massif to form Ol-T.

We estimated that the contribution of mantle assimilation on the overall composition of the gabbroic sequence at the Atlantis Massif is between 0.05 and 0.65% (calculated considering that Ol-T constitute 5% of recovered rocks and using assimilation estimates from our reactive models). The latter was calculated for the most reactive Ol-T 1 (sample 305-U1309D-247R-3W, 16–18) and approaches estimations based on trace elements bulk compositions (<2%, Godard et al., 2009). Higher values of up to 5% assimilated mantle were deduced after major elements bulk compositions (Godard et al., 2009). In Fig. 13, we report calculated compositions of MORBs after 0.05%, 0.65% and 5% mantle olivine assimilation. Fractional crystallization trends of these melts are compared with evolution of a Primary MORB at low (2 kbar) and high (8 kbar) pressure crystallization. Overall, olivine dissolution increases MgO contents of the melt and decreases its CaO contents (Fig. 13) as expected from previous works (e.g., Lambart et al., 2009; Lissenberg and Dick, 2008). The highest assimilation percentage shifts MORB compositions towards much higher MgO than those predicted by low pressure fractional crystallization. Such MgO and CaO contents can otherwise be reached after crystallization at high pressures, and correspond to compositions predicted for the MORB-type melt in equilibrium with the mineral assemblage of Ol-T 1 (Fig. 13). In contrast, the least reactive Ol-T 2 is in equilibrium with a melt that records significant melt fractionation, again suggesting that olivine assimilation had a minor effect on the composition of this type of Ol-T.

Estimations of mantle assimilation from this study seem to underestimate the extent of the reactive process compared to the Godard et al. (2009) estimates. This may be related to the fact that calculations were done at extremely local scale, and that our sampling may lack areas where olivine dissolution was much stronger, as predicted by bulk rock compositions. Our calculations provide a minimum estimate of the extent of mantle assimilation.

7. Conclusions

Major and trace element mineral compositions and reactive percolation modeling demonstrate that olivine from U1309D Ol-T is of impregnated mantle origin. Textures and olivine compositions are locally inherited from the heterogeneous precursor. Chemical profiles reveal evidences of reaction and chemical equilibrium. On the other hand, trace elements indicate that element transport has a fundamental role on the re-distribution of the most incompatible elements (e.g., Godard et al., 1995; Vernières et al., 1997) thus controlling their composition in the mineral phases. Detailed analyses of modal and compositional variations of minerals, together with microstructural observations, appear to be suitable criteria to unravel the origin of olivine in Ol-T.

Our results demonstrate that Primary MORB melt are modified during their upward migration by a complex history of interactions with the pre-existing deformed matrix in an open system. First, dissolution of mantle orthopyroxene coupled to minor olivine precipitation cause a shift of melt compositions towards silica saturation. The melt produced is progressively in chemical disequilibrium with mantle material and the melt-rock reaction switches to dissolution of olivine (e.g., Lambart et al., 2009; Saper and Liang, 2014). As a result, the produced MORB melt is enriched in MgO similar to high pressure fractionated melts. It is saturated in olivine and, at decreasing temperature, forms the gabbroic suite surrounding mantle intervals that are preserved at the top of Hole U1309D.

The principle characteristics of reactive Ol-T, inferred from this study, and previous work (Drouin et al., 2009, 2010), are as following:

(i) *Texture and microstructures*. Deformed (high temperature imprint) corroded coarse and medium grained to undeformed fine grained olivine are embayed in poikilitic clinopyroxene and plagioclase. Olivine crystallographic preferred orientations show relatively weak [001] clusters (Drouin et al., 2010) suggesting formation after melt impregnation at high melt/rock ratios (~30%).

(ii) *Mineral modes and chemistry*. Olivine displays opposite correlation between modal contents and concentration of elements generally hosted in olivine (i.e., Mg#, Ni, Mn, Zn, Li), compared to trends predicted by MORB crystallization. Olivine is characterized by wide variations of Ni and Li at constant Mg#. Clinopyroxene and plagioclase have respectively high Mg# and high An, and both are in chemical equilibrium with olivine.

(iii) *Geochemistry*. Similar mineral trace elements compositions characterize all types of Ol-T. Olivine displays strong fractionation of HREE to MREE with absolute values higher than associated mantle rocks and gabbros (Rampone et al., 2016). Olivine also shows enrichments in the most incompatible elements (i.e., HFSE) that seem to complement plagioclase compositions (Zr-Hf). Clinopyroxene cores do not display Eu negative anomalies. Calculated melts in equilibrium with clinopyroxene and plagioclase have trace elements comparable to Primary MORBs (Drouin et al., 2009) and are in equilibrium with olivine, except for MREE and LREE.
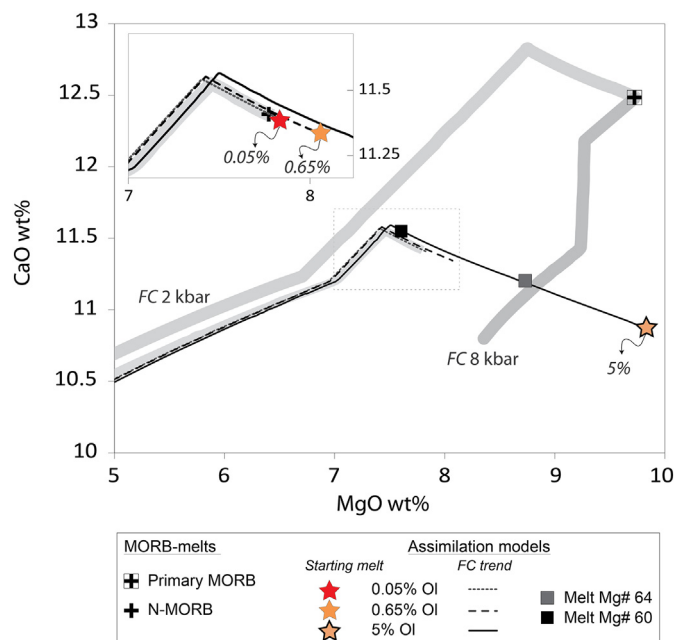
This work reveals that assimilation of mantle olivine accounts for local change of MORB compositions towards relatively primitive compositions. Up to 5% mantle component was assimilated at the Atlantis Massif. The high Mg# bulk Hole U1309D (Godard et al., 2009) indicate that the resulting reacted MORBs are likely those that formed the crustal sequence from troctolitic gabbro to olivine gabbro, gabbro and oxide gabbro recovered at Atlantis Massif. The downhole bulk compositions point to low pressure crystallization (Godard et al., 2009), indicating

Fig. 13. MgO (wt%) versus CaO (wt%) of melts calculated after fractional crystallization as predicted by Petrolog3 (see Fig. 5 for details on the model) at 2 kbar for (i) Primary MORB and N-MORB (thick light grey lines; Supplementary Material Table S6), (ii) melts after 0.05%, 0.65%, 5% of assimilated olivine, calculated using N-MORB as starting melt (Supplementary Material Table S6). Also shown is the liquid line of the primary MORB fractionating at pressures of 8 kbar.

that melt-rock interactions at Site U1309 did not shift MORB compositions towards apparent high pressure fractionation trends as, conversely, observed elsewhere (e.g., Lissenberg and Dick, 2008; Paquet et al., 2016). The complex reactive history that MORB melts record at Atlantis Massif might represent the missing link between mantle relicts, reactive Ol-Ts and cumulate gabbros drilled at IODP Hole U1309D.

Acknowledgements

Appendix A. Supplementary data

Supplementary data to this article can be found online at https://doi.org/10.1016/j.lithos.2018.01.012.

References

Arai, S., Matsukage, K., 1996. Petrology of gabbro-troctolite-peridotite complex from Hess Deep, equatorial pacific: implications for mantle-melt interaction within the oceanic lithosphere. Proc. Ocean Drill. Program Sci. Results 147:135–155. https://doi.org/10.2973/odp.proc.sr.147.008.1996.
Arai, S., Matsukage, K., Isobe, E., Vysotskiy, S., 1997. Concentration of incompatible elements in oceanic mantle: effect of melt/wall interaction in stagnant or failed melt conduits within peridotite. Geochim. Cosmochim. Acta 61, 671–675.
Basch, V., Rampone, E., Crispini, L., Ferrando, C., Ildefonse, B., Godard, M., 2018. From mantle peridotites to hybrid troctolites: textural and chemical evolution during melt-rock interaction history (Mt. Maggiore, Corsica, France). Lithos https://doi.org/10.1016/j.lithos.2018.02.025.
Beattie, P., Ford, C., Russell, D., 1991. Partition coefficients for olivine-melt and orthopyroxene-melt systems. Contributions to Mineralogy and Petrology 109:212–224. https://doi.org/10.1007/BF00306480.
Bédard, J.H., 1993. Oceanic crust as a reactive filter: synkinematic intrusion, hybridization, and assimilation in an ophiolitic magma chamber, western Newfoundland. Geology 21, 77–80.
Bédard, J.H., 2005. Partitioning coefficients between olivine and silicate melts. Lithos 83:394–419. https://doi.org/10.1016/j.lithos.2005.03.011.
Bédard, J.H., 2015. Ophiolitic magma chamber processes, a perspective from the Canadian Appalachians. In: Charlier, B., Namur, O., Latypov, R., Tegner, C. (Eds.), Layered Intrusions. Springer, Berlin, pp. 693–732.
Bédard, J.H., Hebert, R., Berclaz, A., Varfalvy, V., 2000. Syntexis and the genesis of lower oceanic crust. In: Dilek, Y., Moores, E.M., Elthon, D., Nicolas, A. (Eds.), Ophiolites and Oceanic Crust: New Insights From Field Studies and the Ocean Drilling Program, Special Paper. vol. 349. Geological Society of America, pp. 105–119.
Bedini, R.M., Bodinier, J.-L., Vernières, J., 2002. Numerical simulation of Fe-Mg partitioning during melting and melt-rock interactions in the upper mantle. Extended Abstracts, Proceedings of 4th International Orogenic Lherzolites and Mantle Processes Conference. Samani, Japan (unpublished).
Blackman, D.K., Ildefonse, B., John, B.E., Ohara, Y., Miller, D.J., MacLeod, C.J., Expedition 304/305 Scientists, 2006. Expedition 304/305. Proceedings of the Integrated Ocean Drilling Program 304/305 https://doi.org/10.2204/iodp.proc.304305.101.2006.
Blackman, D.K., Ildefonse, B., John, B.E., et al., 2011. Drilling constraints on lithospheric accretion and evolution at Atlantis Massif, Mid-Atlantic Ridge 30N. J. Geophys. Res. Solid Earth 116:1–25. https://doi.org/10.1029/2010JB007931.
Blackman, D.K., Karson, J.A., Kelley, D.S., Cann, J.R., Früh-Green, G.L., Gee, J.S., Hurst, S.D., John, B.E., Morgan, J., Nooner, S.L., Ross, D.K., Schroeder, T.J., Williams, E.A., 2002. Geology of the Atlantis Massif (Mid-Atlantic Ridge, 30°N): implications for the evolution of an ultramafic oceanic core complex. Mar. Geophys. Res. 23:443–469. https://doi.org/10.1023/B:MARI.0000018232.14085.75.
Borghini, G., Rampone, E., 2007. Postcumulus processes in oceanic-type olivine-rich cumulates: the role of trapped melt crystallization versus melt/rock

interaction. Contrib. Mineral. Petrol. 154:619–633. https://doi.org/10.1007/s00410-007-0217-5.
Boudier, F., Nicolas, A., 1995. Nature of the Moho transition zone in the Oman Ophiolite. J. Petrol. 36, 777–796.
Bowen, N.L., 1928. The Evolution of the Igneous Rocks. Dover, New York, N.Y. (332 pp.).
Cann, J.R., Blackman, D.K., Smith, D.K., McAllister, E., Janssen, B., Mello, S., Avgerinos, E., Pascoe, A.R., Escartin, J., 1997. Corrugated slip surfaces formed at ridge–transform intersections on the Mid-Atlantic Ridge. Nature https://doi.org/10.1038/385329a0.
Cannat, M., Mével, C., Maia, M., Deplus, C., Durand, C., Gente, P., Agrinier, P., Belarouchi, A., Dubuisson, G., Humler, E., Reynolds, J., 1995. Thin crust, ultramafic exposures, and rugged faulting patterns at the Mid-Atlantic Ridge (22°–24°N). Geology 23:49–52. https://doi.org/10.1130/0091-7613(1995)023<0049:TCUEAR>2.3.CO;2.
Chakraborty, S., 2008. Diffusion in solid silicates: a tool to track timescales of processes comes of age. Annu. Rev. Earth Planet. Sci. 36:153–190. https://doi.org/10.1146/annurev.earth.36.031207.124125.
Collier, M.L., Kelemen, P.B., 2010. The case for reactive crystallization at mid-ocean ridges. J. Petrol. 51:1913–1940. https://doi.org/10.1093/petrology/egq043.
Coogan, L.A., 2014. The lower oceanic crust. In: Turekian, K.K., Holland, K.D. (Eds.), Treatise on Geochemistry, Second edition 4.14 Elsevier, Amsterdam:pp. 497–541 https://doi.org/10.1016/B978-0-08-095975-7.00316-8.
Coogan, L.A., Jenkin, G.R.T., Wilson, R.N., 2002. Constraining the cooling rate of the lower oceanic crust: a new approach applied to the Oman ophiolite. Earth Planet. Sci. Lett. 199, 10.
Crank, J., 1975. The Mathematics of Diffusion. Second edition. Oxford University Press Ely House, London W.I.
Danyushevsky, L.V., Plechov, P., 2011. Petrolog3: Integrated software for modeling crystallization processes. Geochemistry, Geophysics, Geosystems 12. https://doi.org/10.1029/2011GC003516.
De Hoog, J.C.M., Gall, L, Cornell, D.H., 2010. Trace-element geochemistry of mantle olivine and application to mantle petrogenesis and geothermobarometry. Chem. Geol. 270:196–215. https://doi.org/10.1016/j.chemgeo.2009.11.017.
DePaolo, D.J., 1981. Trace element and isotopic effects of combined wallrock assimilation and fractional crystallization. Earth Planet. Sci. Lett. 53, 189–202.
D'Errico, M.E., Warren, J.M., Godard, M., 2016. Evidence for chemically heterogeneous Arctic mantle beneath the Gakkel Ridge. Geochim. Cosmochim. Acta 174:291–312. https://doi.org/10.1016/j.gca.2015.11.017.
Dick, H.J.B., 1989. Abyssal peridotites, very slow spreading ridges and ocean ridge magmatism. Geol. Soc. Lond., Spec. Publ. 42:71–105. https://doi.org/10.1144/GSL.SP.1989.042.01.06.
Dick, H.J.B., Natland, J.H., Alt, J.C., et al., 2000. A long in-situ section of the lower ocean crust: results of ODP Leg 176 drilling at the Southwest Indian Ridge. Earth Planet. Sci. Lett. 179:31–51. https://doi.org/10.1016/S0012-821X(00)00102-3.
Dick, H.J.B., Ozawa, K., Meyer, P.S., Niu, Y., Robinson, P.T., Constantin, M., Hebert, R., Maeda, J., Natland, J.H., Hirth, J.G., Mackie, S.M., 2002. Primary silicate mineral chemistry of a 1.5-km section of very slow spreading lower ocean crust: ODP Hole 753B, Southwest Indian Ridge. Proceedings of the Ocean Drilling Program 176, 1–61.
Dijkstra, A.H., Barth, M.G., Drury, M.R., Mason, P.R.D., Vissers, R.L.M., 2003. Diffuse porous melt flow and melt-rock reaction in the mantle lithosphere at a slow-spreading ridge: a structural petrology and LA-ICP-MS study of the Othris Peridotite Massif (Greece). Geochem. Geophys. Geosyst. 4:8613. https://doi.org/10.1029/2001GC000278.
Dohmen, R., Becker, H.W., Chakraborty, S., 2007. Fe-Mg diffusion in olivine I: experimental determination between 700 and 1,200 °C as a function of composition, crystal orientation and oxygen fugacity. Phys. Chem. Miner. 34:389–407. https://doi.org/10.1007/s00269-007-0157-7.
Dohmen, R., Chakraborty, S., 2007. Fe-Mg diffusion in olivine II: point defect chemistry, change of diffusion mechanisms and a model for calculation of diffusion coefficients in natural olivine. Phys. Chem. Miner. 34:409–430. https://doi.org/10.1007/s00269-007-0158-6.
Dohmen, R., Kasemann, S.A., Coogan, L, Chakraborty, S., 2010. Diffusion of Li in olivine. Part I: experimental observations and a multi species diffusion model. Geochim. Cosmochim. Acta 74:274–292. https://doi.org/10.1016/j.gca.2009.10.016.
Drouin, M., Godard, M., Ildefonse, B., Bruguier, O., Garrido, C.J., 2009. Geochemical and petrographic evidence for magmatic impregnation in the oceanic lithosphere at Atlantis Massif, Mid-Atlantic Ridge (IODP Hole U1309D, 30°N). Chem. Geol. 264:71–88. https://doi.org/10.1016/j.chemgeo.2009.02.013.
Drouin, M., Ildefonse, B., Godard, M., 2010. A microstructural imprint of melt impregnation in slow spreading lithosphere: olivine-rich troctolites from the Atlantis Massif, Mid-Atlantic Ridge, 30°N, IODP Hole U1309D. Geochem. Geophys. Geosyst. 11:1–21. https://doi.org/10.1029/2009GC002995.
Elthon, D., 1979. High magnesia liquids as the parental magma for ocean floor basalts. Nature 278:514–518. https://doi.org/10.1017/CBO9781107415324.004.
Evans, T.M., Hugh, H.S., Tuff, J., 2008. The influence of melt composition on the partitioning of REEs, Y, Sc, Zr and Al between forsterite and melt in the system CMAS. Geochim. Cosmochim. Acta 72:5708–5721. https://doi.org/10.101-6/j.gca.2008.09.017.
Gale, A., Dalton, C.A., Langmuir, C.H., Su, Y., Schilling, J.G., 2013. The mean composition of ocean ridge basalts. Geochem. Geophys. Geosyst. 14:489–518. https://doi.org/10.1029/2012GC004334.
Garrido, C.J., Bodinier, J.L., Alard, O., 2000. Incompatible trace element partitioning and residence in anhydrous spinel peridotites and websterites from the Ronda orogenic peridotite. Earth Planet. Sci. Lett. 181:341–358. https://doi.org/10.1016/S0012-821X(00)00201-6.
Gast, P.W., 1968. Trace element fractionation and the origin of tholeiitic and alkaline magma types. Geochim. Cosmochim. Acta 32, 1057.
Godard, M., Awaji, S., Hansen, H., Hellebrand, E., Brunelli, D., Johnson, K., Yamasaki, T., Maeda, J., Abratis, M., Christie, D., Kato, Y., Mariet, C., Rosner, M., 2009. Geochemistry of a long in-situ section of intrusive slow-spread oceanic lithosphere: results from

IODP Site U1309 (Atlantis Massif, 30°N Mid-Atlantic-Ridge). Earth Planet. Sci. Lett. 279:110–122. https://doi.org/10.1016/j.epsl.2008.12.034.

Godard, M., Bodinier, J.-L., Vasseur, G., 1995. Effects of mineralogical reactions on trace element redistributions in mantle rocks during percolation processes: a chromatographic approach. Earth Planet. Sci. Lett. 133:449–461. https://doi.org/10.1016/0012-821X(95)00104-K.

Godard, M., Lagabrielle, Y., Alard, O., Harvey, J., 2008. Geochemistry of the highly depleted peridotites drilled at ODP Sites 1272 and 1274 (fifteen-twenty Fracture Zone, Mid-Atlantic Ridge): implications for mantle dynamics beneath a slow spreading ridge. Earth Planet. Sci. Lett. 267:410–425. https://doi.org/10.1016/j.epsl.2007.11.058.

Grimes, C.B., John, B.E., Cheadle, M.J., Wooden, J.L., 2008. Protracted construction of gabbroic crust at a slow spreading ridge: Constraints from 206Pb/238U zircon ages from Atlantis Massif and IODP Hole U1309D (30°N, MAR). Geochem. Geophys. Geosyst. 9. https://doi.org/10.1029/2008GC002063.

Grove, T.L., Kinzler, R.J., Bryan, W.B., 1992. Mantle flow and melt generation at mid-ocean ridges: fractionation of mid-ocean ridge basalt (MORB). In: Morgan, J.P., Blackman, D.B., Sinton, J.M. (Eds.), Mantle Flow and Melt Generation at Mid-ocean Ridges, Geophysical Monograph Series. vol. 71. AGU, Washington, D. C:pp. 281–311. https://doi.org/10.1029/GM071p0281.

Hart, S.R., Davis, K.E., 1978. Nickel partitioning between olivine and silicate melt. Earth Planet. Sci. Lett. 40:203–219. https://doi.org/10.1016/j.pcad.2011.11.003.

Hebert, R., Constantin, M., Robinson, P.T., 1991. Primary mineralogy of Leg 118 gabbroic rocks and their place in the spectrum of oceanic mafic igneous rocks. Proceeding of the ocean drilling program Leg 118. Sci. Results 118, 3–20.

Higgie, K., Tommasi, A., 2012. Feedbacks between deformation and melt distribution in the crust–mantle transition zone of the Oman ophiolite. Earth Planet. Sci. Lett. 359–360:61–72. https://doi.org/10.1016/j.epsl.2012.10.003.

Holness, M.B., Anderson, A.T., Martin, V.M., Maclennan, J., Passmore, E., Schwindinger, K., 2007. Textures in partially solidified crystalline nodules: a window into the pore structure of slowly cooled mafic intrusions. J. Petrol. 48:1243–1264. https://doi.org/10.1093/petrology/egm016.

Ildefonse, B., Abe, N., Godard, M., Morris, A., Teagle, D.A.H., Umino, S., 2014. Formation and evolution of oceanic lithosphere: new insights on crustal structure and igneous geochemistry from ODP/IODP Sites 1256, U1309, and U1415. Dev. Mar. Geol. https://doi.org/10.1016/B978-0-444-62617-2.00017-7.

Ildefonse, B., Blackman, D.K., John, B.E., et al., 2007. Oceanic core complexes and crustal accretion at slow-spreading ridges. Geology 35:623–626. https://doi.org/10.1130/G23531A.1.

Jollands, M.C., Hermann, J., O'Neill, H.S.C., Spandler, C., Padrón-Navarta, J.A., 2016. Diffusion of Ti and some divalent cations in olivine as a function of temperature, oxygen fugacity, chemical potentials and crystal orientation. J. Petrol. 57:1983–2010. https://doi.org/10.1093/petrology/egw067.

Johnson, K.T.M., Dick, H.J.B., Shimizu, N., 1990. Melting in the Oceanic Upper Mantle: an Ion Microprobe Study of Diopsides in Abyssal Peridotites. Journal of Geophysical Research 95 (B3), 2661–2678.

Kelemen, P.B., Hirth, G., Shimizu, N., Spiegelman, M., Dick, H.J., 1997. A review of melt migration processes in the adiabatically upwelling mantle beneath oceanic spreading ridges. Philos. Trans. R. Soc. London, Ser. A 355:283–318. https://doi.org/10.1098/rsta.1997.0010.

Kinzler, R.J., 1997. Melting of mantle peridotite at pressures approaching the spinel to garnet transition: application to mid-ocean ridge basalt petrogenesis. Journal of Geophysical Research 102:853–874. https://doi.org/10.1016/S0377-0273(00)00182-7.

Kvassnes, A.J.S., Grove, T.L., 2008. How partial melts of mafic lower crust affect ascending magmas at oceanic ridges. Contrib. Mineral. Petrol. 156:49–71. https://doi.org/10.1007/s00410-007-0273-x.

Lambart, S., Laporte, D., Schiano, P., 2009. An experimental study of focused magma transport and basalt-peridotite interactions beneath mid-ocean ridges: implications for the generation of primitive MORB compositions. Contrib. Mineral. Petrol. 157:429–451. https://doi.org/10.1007/s00410-008-0344-7.

Langmuir, C.H., 1989. Geochemical consequences of in situ crystallization. Nature https://doi.org/10.1038/340199a0.

Liang, Y., 2003. Kinetics of crystal-melt reaction in partially molten silicates: 1. Grain scale processes. Geochem. Geophys. Geosyst. 4. https://doi.org/10.1029/2002GC000375.

Lissenberg, C.J., Dick, H.J.B., 2008. Melt-rock reaction in the lower oceanic crust and its implications for the genesis of mid-ocean ridge basalt. Earth Planet. Sci. Lett. 271:311–325. https://doi.org/10.1016/j.epsl.2008.04.023.

Lissenberg, C.J., MacLeod, C.J., Howard, K.A., Godard, M., 2013. Pervasive reactive melt migration through fast-spreading lower oceanic crust (Hess Deep, equatorial Pacific Ocean). Earth Planet. Sci. Lett. 361:436–447. https://doi.org/10.1016/j.epsl.2012.11.012.

Miller, D.J., Abratis, M., Christie, D., Drouin, M., Godard, M., Ildefonse, B., Maeda, J., Weinsteiger, A., Yamasaki, T., Suzuki, Y., Niino, A., Sato, Y., Takeda, F., 2009. Data report: microprobe analyses of primary mineral phases from Site U1309, Atlantis Massif, IODP expedition 304/305. Proceedings of the Integrated Ocean Drilling Program 304/305 https://doi.org/10.2204/iodp.proc.304305.202.2009.

Navon, O., Stolper, E.M., 1987. Geochemical consequences of melt percolation - the upper mantle as a chromatographic column. J. Geol. 95, 285–307.

O'Driscoll, B., Donaldson, C.H., Troll, V.R., Jerram, D.A., Emeleus, C.H., 2007. An origin for harrisitic and granular olivine in the Rum layered suite, NW Scotland: a crystal size distribution study. J. Petrol. 48:253–270. https://doi.org/10.1093/petrology/egl059.

O'Hara, M.J., 1965. Primary magmas and the origin of basalts. Scott. J. Geol. 1:19–40. https://doi.org/10.1144/sjg01010019.

O'Hara, M.J., 1977. Geochemical evolution during fractional crystallization of a periodically refilled magma chamber. Nature 266, 503.

O'Neill, H.S.C., Jenner, F.E., 2012. The global pattern of trace-element distributions in ocean floor basalts. Nature 491:698–704. https://doi.org/10.1038/nature11678.

Paquet, M., Cannat, M., Brunelli, D., Hamelin, C., Humler, E., 2016. Effect of melt/mantle interactions on MORB chemistry at the easternmost Southwest Indian Ridge (61°–67°E). Geochem. Geophys. Geosyst. 17. https://doi.org/10.1002/2016GC006385.

Pearce, N.J.G., Perkins, W.T., Westgate, J.A., Gorton, M.P., Jackson, S.E., Neal, C.R., Chenery, S.P., 1997. A compilation of new and published major and trace element data for NIST SRM 610 and NIST SRM 612 glass reference materials. Geostandards Newsletter: The Journal of Geostandards and Geoanalysis 21 (1), 115–144.

Pec, M., Holtzman, B., Zimmerman, M., Kohlstedt, D., 2017. Reaction infiltration instabilities in mantle rocks: An experimental investigation. Journal of Petrology 58 (5):979–1003. https://doi.org/10.1093/petrology/egx043.

Petry, C., Chakraborty, S., Palme, H., 2004. Experimental determination of Ni diffusion coefficients in olivine and their dependence on temperature, composition, oxygen fugacity, and crystallographic orientation. Geochim. Cosmochim. Acta 68:4179–4188. https://doi.org/10.1016/j.gca.2004.02.024.

Presnall, D., Hoover, J.D., 1987. High pressure phase equilibrium constraints on the origin of mid-ocean ridge basalts. In: Mysen, B.O. (Ed.), Magmatic Processes: Physicochemical Principles. Special Publication-Geochemical Society, pp. 75–89.

Rampone, E., Borghini, G., Godard, M., Ildefonse, B., Crispini, L., Fumagalli, P., 2016. Melt/rock reaction at oceanic peridotite/gabbro transition as revealed by trace element chemistry of olivine. Geochim. Cosmochim. Acta 190:309–331. https://doi.org/10.1016/j.gca.2016.06.029.

Remmert, P., Dohmen, R., Chakraborty, S., 2008. Diffusion of REE, Hf and Sr in Olivine. EOS Transactions American Geophysical Union (Fall Meeting Supplementary, Abstract MR33A-1844). https://doi.org/10.1029/2001GC000205.

Renna, M.R., Tribuzio, R., Ottolini, L., 2016. New perspectives on the origin of olivine-rich troctolites and associated harrisites from the Ligurian ophiolites (Italy). J. Geol. Soc. Lond. 173:916–932. https://doi.org/10.1144/jgs2015-135.

Ross, D.K., Elthon, D., 1997. Cumulus and postcumulus crystallization in the oceanic crust: major- and trace-element geochemistry of Leg 153 gabbroic rocks. Proc. Ocean Drill. Program Sci. Results 153:333–353. https://doi.org/10.2973/odp.proc.sr.153.023.1997.

Sanfilippo, A., Tribuzio, R., 2011. Melt transport and deformation history in a nonvolcanic ophiolitic section, northern Apennines, Italy: Implications for crustal accretion at slow spreading settings. Geochemistry, Geophysics, Geosystems 12:1–34. https://doi.org/10.1029/2010GC003429.

Sanfilippo, A., Tribuzio, R., 2013. Building of the deepest crust at a fossil slow-spreading centre (Pineto gabbroic sequence, Alpine Jurassic ophiolites). Contrib. Mineral. Petrol. 165:705–721. https://doi.org/10.1007/s00410-012-0831-8.

Sanfilippo, A., Morishita, T., Kumagai, H., Nakamura, K., Okino, K., Hara, K., Tamura, A., Arai, S., 2015. Hybrid troctolites from mid-ocean ridges: inherited mantle in the lower crust. Lithos 232:124–130. https://doi.org/10.1016/j.lithos.2015.06.025.

Sanfilippo, A., Tribuzio, R., Tiepolo, M., 2014. Mantle-crust interactions in the oceanic lithosphere: constraints from minor and trace elements in olivine. Geochim. Cosmochim. Acta 141:423–439. https://doi.org/10.1016/j.gca.2014.06.012.

Sanfilippo, A., Tribuzio, R., Tiepolo, M., Berno, D., 2015. Reactive flow as dominant evolution process in the lowermost oceanic crust: evidence from olivine of the Pineto ophiolite (Corsica). Contrib. Mineral. Petrol. 170. https://doi.org/10.1007/s00410-015-1194-8.

Saper, L., Liang, Y., 2014. Formation of plagioclase-bearing peridotite and plagioclase-bearing wehrlite and gabbro suite through reactive crystallization: an experimental study. Contrib. Mineral. Petrol. 167:1–16. https://doi.org/10.1007/s00410-014-0985-7.

Seyler, M., Lorand, J.P., Dick, H.J.B., Drouin, M., 2007. Pervasive melt percolation reactions in ultra-depleted refractory harzburgites at the Mid-Atlantic Ridge, 15° 20′N: ODP Hole 1274A. Contrib. Mineral. Petrol. 153:303–319. https://doi.org/10.1007/s00410-006-0148-6.

Shaw, D.M., 1970. Trace element fractionation during anatexis. Geochim. Cosmochim. Acta 40, 73.

Spandler, C., O'Neill, H.S.C., 2010. Diffusion and partition coefficients of minor and trace elements in San Carlos olivine at 1,300°C with some geochemical implications. Contributions to Mineralogy and Petrology 159:1–28. https://doi.org/10.1007/s00410-009-0456-8.

Suhr, G., Hellebrand, E., Johnson, K., Brunelli, D., 2008. Stacked gabbro units and intervening mantle: a detailed look at a section of IODP leg 305, hole U1309D. Geochem. Geophys. Geosyst. 9. https://doi.org/10.1029/2008GC002012.

Sun, C., Liang, Y., 2014. An assessment of subsolidus re-equilibration on REE distribution among mantle minerals olivine, orthopyroxene, clinopyroxene, and garnet in peridotites. Chem. Geol. 372:80–91. https://doi.org/10.1016/j.chemgeo.2014.02.014.

Sun, S.-s., McDonough, W.F., 1989. Chemical and isotopic systematics of oceanic basalts: implications for mantle composition and processes. Geol. Soc. Lond., Spec. Publ. 42:313–345. https://doi.org/10.1144/GSL.SP.1989.042.01.19.

Tamura, A., Arai, S., Ishimaru, S., Andal, E.S., 2008. Petrology and geochemistry of peridotites from IODP Site U1309 at Atlantis Massif, MAR 30° N: micro- and macroscale melt penetrations into peridotites. Contrib. Mineral. Petrol. 155:491–509. https://doi.org/10.1007/s00410-007-0254-0.

Tartarotti, P., Susini, S., Nimis, P., Ottolini, L., 2002. Melt migration in the upper mantle along the Romanche Fracture Zone (Equatorial Atlantic). Lithos 63:125–149. https://doi.org/10.1016/S0024-4937(02)00116-0.

Tommasi, A., Mainprice, D., Gilles, C., Yvan, C., 2000. Viscoplastic self-consistent and equilibrium-based modeling of olivine lattice preferred orientations: implications for the upper mantle seismic anisotropy. J. Geophys. Res. 105:7893–7908. https://doi.org/10.1029/1999JB900411.

Toramaru, A., Fujii, N., 1986. Connectivity of melt phase in a partially molten peridotite. J. Geophys. Res. 91, 9239–9252.

Turcotte, D.L., Morgan, J.P., 1992. The physics of magma migration and mantle flow beneath a mid-ocean ridge. In: Morgan, J.P., Blackman, D.B., Sinton, J.M. (Eds.), Mantle

Flow and Melt Generation at Mid-Ocean Ridges, Geophysical Monograph Series. vol. 71. AGU, Washington, D. C:pp. 155–182. https://doi.org/10.1029/GM071p0155.

Van Achterberg, E., Ryan, C.G., Jackson, S.E., Griffin, W., 2001. Data reduction software for LA-ICP-MS. In: Sylvester, P. (Ed.), Laser ablation ICP-MS in the Earth Science. Mineralogical Association of Canada, pp. 239–243.

Van den Bleeken, G., Müntener, O., Ulmer, P., 2011. Melt variability in percolated peridotite: an experimental study applied to reactive migration of tholeiitic basalt in the upper mantle. Contrib. Mineral. Petrol. 161:921–945. https://doi.org/10.1007/s00410-010-0572-5.

Vernières, J., Godard, M., Bodinier, J.-L., 1997. A plate model for the simulation of trace element fractionation during partial melting and magma transport in the Earth's upper mantle. J. Geophys. Res. Solid Earth 102, 24771–24784.

Villiger, S., Ulmer, P., Müntener, O., 2007. Equilibrium and fractional crystallization experiments at 0.7 GPa; the effect of pressure on phase relations and liquid compositions of tholeiitic magmas. J. Petrol. 48:159–184. https://doi.org/10.1093/petrology/egl058.

von Bargen, N., Waff, H.S., 1986. Permeabilities, interfacvial areas and curvatures of partially molten systems: results of numerical computations of equilibrium microstructures. J. Geophys. Res. 91, 9261–9276.

Workman, R.K., Hart, S.R., 2005. Major and trace element composition of the depleted MORB mantle (DMM). Earth Planet. Sci. Lett. 231:53–72. https://doi.org/10.1016/j.epsl.2004.12.005.

Yoshinobu, A.S., Hirth, G., 2002. Microstructural and experimental constraints on the rheology of partially molten gabbro beneath oceanic spreading centers. Journal of Structural Geology 24:1101–1107. https://doi.org/10.1016/S0191-8141(01)00094-3.